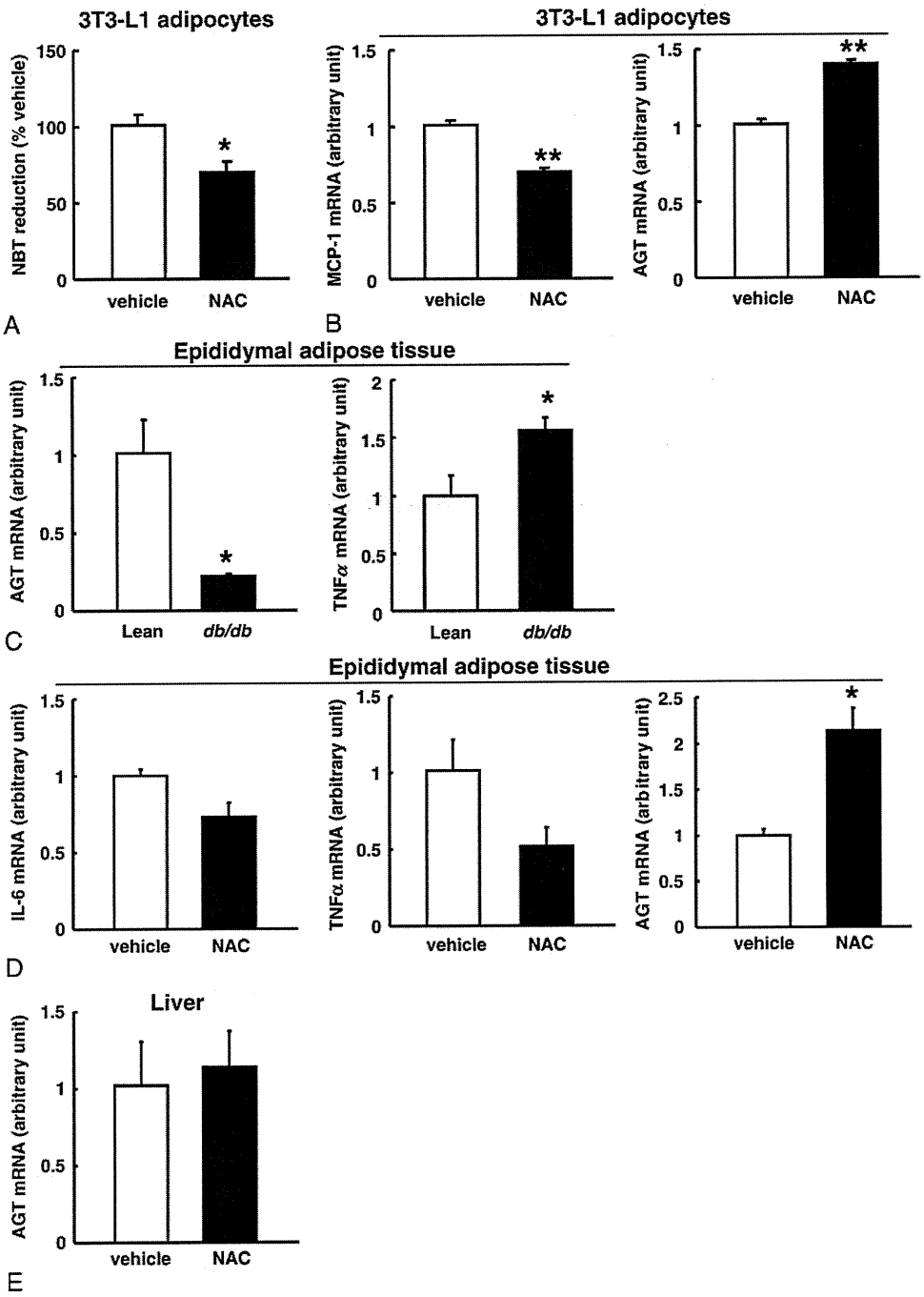

Fig. 5. Effect of antioxidant treatment on the expression and secretion of AGT in the adipocytes. A, Suppression of ROS generation in the 3T3-L1 adipocytes treated with NAC (10 mmol/L) for 10 days (n = 3). The ROS was estimated by the NBT assay. B, The MCP-1 and AGT mRNA levels in the 3T3-L1 adipocytes incubated with NAC (10 mmol/L) (n = 8). The mRNA level was examined by real-time PCR and normalized to that of 18S rRNA. Results are representatives of at least 3 independent experiments. C, Comparison of the AGT and TNFα mRNA levels between 10-week-old male *db/db* mice (n = 4; mean body weight, 48 ± 1.5 g) and their lean littermates (n = 4; mean body weight, 28 ± 1.0 g) in epididymal adipose tissue. D, The level of IL-6, TNFα, and AGT mRNA in the epididymal adipose tissue depots of obese *db/db* mice treated with NAC (150 mg/kg body weight) or vehicle (phosphate-buffered saline) once daily for 1 week (n = 3). E, The AGT mRNA level in the liver of obese *db/db* mice treated with NAC or vehicle for 1 week (n = 3). The mRNA level was examined by real-time PCR and normalized to that of cyclophilin mRNA. The data are expressed as the mean ± SE. $^{*}P < .05$ and $^{**}P < .01$ as compared with the control value.

AGT expression is decreased in obese adipose tissue. Reactive oxygen species (H_2O_2) decreased AGT expression in both 3T3-L1 adipocytes and primary adipocytes (Fig. 4). On the other hand, elimination of ROS with antioxidant increased AGT expression not only in hypertrophied 3T3-L1 adipocytes but also in adipose tissue from obese mice (Fig. 5). The oxidative stress–mediated decrease in adipose AGT is reproduced in our various experiments.

Several studies have suggested the augmentation of AGT by oxidative stress in the liver and kidney. In the liver, angiotensin II is known to enhance AGT expression via ROS generation [23], resulting in a positive feedback loop of AGT production [43]. In addition, oxidative stress mediated by hyperglycemia and hypertension has been shown to augment the expression of AGT in the rodent kidney [25,26]. In turn, elevated expression of AGT has been shown to activate renal RAS and considerably contribute to renal injury [26]. On the other hand, our data support a notion that oxidative stress "decreases" expression and secretion of AGT in obese adipose tissue, implying that regulation of AGT in adipose tissue may be distinct from other tissues in response to oxidative stress.

The clinical or pathophysiologic implications of decreased AGT in obese adipose tissue still remain unclear. Although further studies are warranted, the notion that adipose tissue RAS is involved in the control of adipogenesis and adipose tissue mass [44] tempts us to speculate that tissue-specific decrease of AGT in obese adipose tissue may serve as a defense against further exacerbation of adiposity. In obese adipose tissue, exaggerated oxidative stress affects the expression of a variety of genes [17]. Representatively, ROS induces the proinflammatory TNFα but suppresses the anti-inflammatory adiponectin in murine adipose tissue [17]. Glutathione peroxidase 3 (GPx3), an antioxidant enzyme secreted from the adipose tissue and kidney, is known to be decreased by oxidative stress exclusively in adipose tissue in obese *db/db* mice [38]. Notably, in vivo administration of an antioxidant was shown to rescue the decrease in GPx3 expression only in adipose tissue, but not in the kidney [38]. In this context, AGT shares close similarity with adiponectin and GPx3 in terms of the response to oxidative stress in adipose tissue.

Tissue-specific dysregulation of AGT has also been observed in inflammatory response [45,46]. Hepatic AGT is shown to increase by inflammatory stimuli via the acute-phase responsive element (APRE) on the promoter region of the AGT gene [43,47]. In rats treated with lipopolysaccharide, AGT mRNA level was shown to increase in the liver, aorta, and adrenal gland, but remained unchanged in the kidney [45]. Furthermore, in transgenic mice with cardioselective overexpression of TNFα, expression of AGT was decreased exclusively in the heart [46]. In the present study, we demonstrated that TNFα decreased the expression and secretion of AGT in 3T3-L1 adipocytes (Fig. 3). Considering that chronic, low-grade inflammation is a manifestation of obese adipose tissue [48,49], our results suggest that AGT is inversely regulated by inflammation in obese adipose tissue.

Previous works have raised a possibility that the inflammatory responses to AGT in adipose tissue and liver are controlled by distinct mechanisms [50]. In cultured adipocytes, inflammatory signals transcriptionally decrease AGT by the inhibition of APRE [50]; however, in cultured hepatocytes, nuclear factor–κB signaling augments AGT by the activation of APRE [47]. Importantly, the intracellular signaling involved in oxidative stress and inflammation interact and share, at least in part, common pathways in a tissue-specific manner [18,19]. In this context, tissue-specific dysregulation of AGT by oxidative stress is reminiscent of the case in inflammatory signals; and a possible link between the dysregulation of AGT and oxidative stress in obese adipose tissue may provide a fresh clue to dissect the pathophysiology of obesity. For example, we would suggest the one possibility that oxidative stress–induced suppression of adipose tissue RAS via the decrease in AGT may control adipose tissue function including adipocyte differentiation, lipolysis, and local blood flow [44].

In summary, the present study demonstrates for the first time that oxidative stress dysregulates AGT in obese adipose tissue in humans and rodents as well as in cultured adipocytes with hypertrophy. Our results support a concept that oxidative stress–dependent decrease in AGT may be a unique facet of dysfunction in obese adipose tissue.

Acknowledgment

We are grateful to A Katsurada (Departments of Medicine and Physiology, and Hypertension and Renal Center of Excellence, Tulane University Health Sciences Center, New Orleans, LA), M Tabuchi (Department of Pharmacology, Kinki University School of Medicine, Osaka-sayama, Japan), M Okada (Department of Internal Medicine, Kobe University Graduate School of Medicine, Kobe, Japan), and M Kasuga (Research Institute, International Medical Center of Japan, Tokyo, Japan) for help and discussion. We also thank A Ryu, S Maki, and M Nagamoto for assistance and Y Kobayashi and T Fukui for discussion.

This work was supported in part by Grants-in-Aid (MEXT, Japan) B2 and S2, Takeda Medical Research Foundation, Smoking Research Foundation, Lilly Research Foundation, Research on Measures for Intractable Diseases (Health and Labor Science Research Grant), Special Coordination Funds for Promoting Science and Technology (JST), Research Grant of National Cardiovascular Center, Sankyo Research Foundation, the Korea Research Foundation Grant (KRF-2008-005-J00203), and the National Research Laboratory Program (ROA-2004-000-10359-0) funded by the Korean Government.

References

[1] Engeli S. Role of the renin-angiotensin-aldosterone system in the metabolic syndrome. Contrib Nephrol 2006;151:122-34.

[2] Rahmouni K, Correia ML, Haynes WG, Mark AL. Obesity-associated hypertension: new insights into mechanisms. Hypertension 2005;45: 9-14.

[3] Dzau VJ. Circulating versus local renin-angiotensin system in cardiovascular homeostasis. Circulation 1988;77(6 Pt 2):I4-I13.

[4] Raizada V, Skipper B, Luo W, Griffith J. Intracardiac and intrarenal renin-angiotensin systems: mechanisms of cardiovascular and renal effects. J Investig Med 2007;55:341-59.

[5] Cassis LA, Saye J, Peach MJ. Location and regulation of rat angiotensinogen messenger RNA. Hypertension 1988;11(6 Pt 2): 591-6.
[6] Giacchetti G, Faloia E, Mariniello B, Sardu C, Gatti C, Camilloni MA, et al. Overexpression of the renin-angiotensin system in human visceral adipose tissue in normal and overweight subjects. Am J Hypertens 2002;15:381-8.
[7] Engeli S, Negrel R, Sharma AM. Physiology and pathophysiology of the adipose tissue renin-angiotensin system. Hypertension 2000;35: 1270-7.
[8] Massiera F, Seydoux J, Geloen A, Quignard-Boulange A, Turban S, Saint-Marc P, et al. Angiotensinogen-deficient mice exhibit impairment of diet-induced weight gain with alteration in adipose tissue development and increased locomotor activity. Endocrinology 2001; 142:5220-5.
[9] Massiera F, Bloch-Faure M, Ceiler D, Murakami K, Fukamizu A, Gasc JM, et al. Adipose angiotensinogen is involved in adipose tissue growth and blood pressure regulation. FASEB J 2001;15:2727-9.
[10] Frederich Jr RC, Kahn BB, Peach MJ, Flier JS. Tissue-specific nutritional regulation of angiotensinogen in adipose tissue. Hypertension 1992;19:339-44.
[11] Boustany CM, Bharadwaj K, Daugherty A, Brown DR, Randall DC, Cassis LA. Activation of the systemic and adipose renin-angiotensin system in rats with diet-induced obesity and hypertension. Am J Physiol Regul Integr Comp Physiol 2004;287:R943-9.
[12] Van Harmelen V, Ariapart P, Hoffstedt J, Lundkvist I, Bringman S, Arner P. Increased adipose angiotensinogen gene expression in human obesity. Obes Res 2000;8:337-41.
[13] Engeli S, Bohnke J, Gorzelniak K, Janke J, Schling P, Bader M, et al. Weight loss and the renin-angiotensin-aldosterone system. Hypertension 2005;45:356-62.
[14] Engeli S, Schling P, Gorzelniak K, Boschmann M, Janke J, Ailhaud G, et al. The adipose-tissue renin-angiotensin-aldosterone system: role in the metabolic syndrome? Int J Biochem Cell Biol 2003;35:807-25.
[15] Keaney Jr JF, Larson MG, Vasan RS, Wilson PW, Lipinska I, Corey D, et al. Obesity and systemic oxidative stress: clinical correlates of oxidative stress in the Framingham Study. Arterioscler Thromb Vasc Biol 2003;23:434-9.
[16] Urakawa H, Katsuki A, Sumida Y, Gabazza EC, Murashima S, Morioka K, et al. Oxidative stress is associated with adiposity and insulin resistance in men. J Clin Endocrinol Metab 2003;88:4673-6.
[17] Furukawa S, Fujita T, Shimabukuro M, Iwaki M, Yamada Y, Nakajima Y, et al. Increased oxidative stress in obesity and its impact on metabolic syndrome. J Clin Invest 2004;114:1752-61.
[18] Stocker R, Keaney Jr JF. Role of oxidative modifications in atherosclerosis. Physiol Rev 2004;84:1381-478.
[19] Grattagliano I, Palmieri VO, Portincasa P, Moschetta A, Palasciano G. Oxidative stress–induced risk factors associated with the metabolic syndrome: a unifying hypothesis. J Nutr Biochem 2008;19:491-504.
[20] Griendling KK, Minieri CA, Ollerenshaw JD, Alexander RW. Angiotensin II stimulates NADH and NADPH oxidase activity in cultured vascular smooth muscle cells. Circ Res 1994;74:1141-8.
[21] Das DK, Maulik N, Engelman RM. Redox regulation of angiotensin II signaling in the heart. J Cell Mol Med 2004;8:144-52.
[22] Sachse A, Wolf G. Angiotensin II–induced reactive oxygen species and the kidney. J Am Soc Nephrol 2007;18:2439-46.
[23] Brasier AR, Jamaluddin M, Han Y, Patterson C, Runge MS. Angiotensin II induces gene transcription through cell-type–dependent effects on the nuclear factor–kappaB (NF-kappaB) transcription factor. Mol Cell Biochem 2000;212:155-69.
[24] Hsieh TJ, Zhang SL, Filep JG, Tang SS, Ingelfinger JR, Chan JS. High glucose stimulates angiotensinogen gene expression via reactive oxygen species generation in rat kidney proximal tubular cells. Endocrinology 2002;143:2975-85.
[25] Brezniceanu ML, Liu F, Wei CC, Tran S, Sachetelli S, Zhang SL, et al. Catalase overexpression attenuates angiotensinogen expression and apoptosis in diabetic mice. Kidney Int 2007;71:912-23.
[26] Miyata K, Ohashi N, Suzaki Y, Katsurada A, Kobori H. Sequential activation of the reactive oxygen species/angiotensinogen/renin-angiotensin system axis in renal injury of type 2 diabetic rats. Clin Exp Pharmacol Physiol 2008;35:922-7.
[27] Houstis N, Rosen ED, Lander ES. Reactive oxygen species have a causal role in multiple forms of insulin resistance. Nature 2006;440:944-8.
[28] Frost SC, Lane MD. Evidence for the involvement of vicinal sulfhydryl groups in insulin-activated hexose transport by 3T3-L1 adipocytes. J Biol Chem 1985;260:2646-52.
[29] Fujimoto M, Masuzaki H, Tanaka T, Yasue S, Tomita T, Okazawa K, et al. An angiotensin II AT1 receptor antagonist, telmisartan augments glucose uptake and GLUT4 protein expression in 3T3-L1 adipocytes. FEBS Lett 2004;576:492-7.
[30] Sakai T, Sakaue H, Nakamura T, Okada M, Matsuki Y, Watanabe E, et al. Skp2 controls adipocyte proliferation during the development of obesity. J Biol Chem 2007;282:2038-46.
[31] Kobori H, Katsurada A, Miyata K, Ohashi N, Satou R, Saito T, et al. Determination of plasma and urinary angiotensinogen levels in rodents by newly developed ELISA. Am J Physiol Renal Physiol 2008;294: F1257-63.
[32] Oliveira HR, Verlengia R, Carvalho CR, Britto LR, Curi R, Carpinelli AR. Pancreatic beta-cells express phagocyte-like NAD(P)H oxidase. Diabetes 2003;52:1457-63.
[33] Saye JA, Cassis LA, Sturgill TW, Lynch KR, Peach MJ. Angiotensinogen gene expression in 3T3-L1 cells. Am J Physiol 1989;256(2 Pt 1): C448-51.
[34] Wajant H, Pfizenmaier K, Scheurich P. Tumor necrosis factor signaling. Cell Death Differ 2003;10:45-65.
[35] Cawthorn WP, Sethi JK. TNF-alpha and adipocyte biology. FEBS Lett 2008;582:117-31.
[36] Kamigaki M, Sakaue S, Tsujino I, Ohira H, Ikeda D, Itoh N, et al. Oxidative stress provokes atherogenic changes in adipokine gene expression in 3T3-L1 adipocytes. Biochem Biophys Res Commun 2006;339:624-32.
[37] Lee H, Lee YJ, Choi H, Ko EH, Kim JW. Reactive oxygen species facilitate adipocyte differentiation by accelerating mitotic clonal expansion. J Biol Chem 2009;284:10601-9.
[38] Lee YS, Kim AY, Choi JW, Kim M, Yasue S, Son HJ, et al. Dysregulation of adipose glutathione peroxidase 3 in obesity contributes to local and systemic oxidative stress. Mol Endocrinol 2008;22:2176-89.
[39] Wang B, Jenkins JR, Trayhurn P. Expression and secretion of inflammation-related adipokines by human adipocytes differentiated in culture: integrated response to TNF-alpha. Am J Physiol Endocrinol Metab 2005;288:E731-40.
[40] Jones BH, Standridge MK, Taylor JW, Moustaid N. Angiotensinogen gene expression in adipose tissue: analysis of obese models and hormonal and nutritional control. Am J Physiol 1997;273(1 Pt 2): R236-42.
[41] Aubert J, Safonova I, Negrel R, Ailhaud G. Insulin down-regulates angiotensinogen gene expression and angiotensinogen secretion in cultured adipose cells. Biochem Biophys Res Commun 1998;250: 77-82.
[42] Harte A, McTernan P, Chetty R, Coppack S, Katz J, Smith S, et al. Insulin-mediated upregulation of the renin angiotensin system in human subcutaneous adipocytes is reduced by rosiglitazone. Circulation 2005;111:1954-61.
[43] Morgan L, Broughton Pipkin F, Kalsheker N. Angiotensinogen: molecular biology, biochemistry and physiology. Int J Biochem Cell Biol 1996;28:1211-22.
[44] Thatcher S, Yiannikouris F, Gupte M, Cassis L. The adipose renin-angiotensin system: role in cardiovascular disease. Mol Cell Endocrinol 2009;302:111-7.
[45] Nyui N, Tamura K, Yamaguchi S, Nakamaru M, Ishigami T, Yabana M, et al. Tissue angiotensinogen gene expression induced by lipopolysaccharide in hypertensive rats. Hypertension 1997;30: 859-67.

[46] Flesch M, Hoper A, Dell'Italia L, Evans K, Bond R, Peshock R, et al. Activation and functional significance of the renin-angiotensin system in mice with cardiac restricted overexpression of tumor necrosis factor. Circulation 2003;108:598-604.
[47] Ron D, Brasier AR, Habener JF. Transcriptional regulation of hepatic angiotensinogen gene expression by the acute-phase response. Mol Cell Endocrinol 1990;74:C97-C104.
[48] Hotamisligil GS, Arner P, Caro JF, Atkinson RL, Spiegelman BM. Increased adipose tissue expression of tumor necrosis factor–alpha in human obesity and insulin resistance. J Clin Invest 1995;95: 2409-15.
[49] Xu H, Barnes GT, Yang Q, Tan G, Yang D, Chou CJ, et al. Chronic inflammation in fat plays a crucial role in the development of obesity-related insulin resistance. J Clin Invest 2003;112:1821-30.
[50] Ron D, Brasier AR, McGehee Jr RE, Habener JF. Tumor necrosis factor–induced reversal of adipocytic phenotype of 3T3-L1 cells is preceded by a loss of nuclear CCAAT/enhancer binding protein (C/EBP). J Clin Invest 1992;89:223-33.

Neurobiology of Disease

A Missense Mutation of the Gene Encoding Voltage-Dependent Sodium Channel ($Na_v1.1$) Confers Susceptibility to Febrile Seizures in Rats

Tomoji Mashimo,[1] Iori Ohmori,[2] Mamoru Ouchida,[3] Yukihiro Ohno,[4] Toshiko Tsurumi,[1] Takafumi Miki,[5] Minoru Wakamori,[6] Shizuka Ishihara,[4] Takashi Yoshida,[6] Akiko Takizawa,[1] Megumi Kato,[7] Masumi Hirabayashi,[7] Masashi Sasa,[8] Yasuo Mori,[5] and Tadao Serikawa[1]

[1]Institute of Laboratory Animals, Graduate School of Medicine, Kyoto University, Kyoto 606-8501, Japan, Departments of [2]Physiology and [3]Molecular Genetics, Graduate School of Medicine, Dentistry, and Pharmaceutical Sciences, Okayama University, Okayama 700-8558, Japan, [4]Laboratory of Pharmacology, Osaka University of Pharmaceutical Sciences, Takatsuki, Osaka 569-1094, Japan, [5]Laboratory of Molecular Biology, Department of Synthetic Chemistry and Biological Chemistry Graduate School of Engineering, Kyoto University, Kyoto 615-8501, Japan, [6]Department of Oral Biology, Graduate School of Dentistry, Tohoku University, Sendai 980-8575, Japan, [7]Center for Genetic Analysis of Behavior, National Institute for Physiological Sciences, Okazaki 444-8587, Japan, and [8]Nagisa Hospital, Hirakata, Osaka 573-1183, Japan

Although febrile seizures (FSs) are the most common convulsive syndrome in infants and childhood, the etiology of FSs has remained unclarified. Several missense mutations of the $Na_v1.1$ channel (SCN1A), which alter channel properties, have been reported in a familial syndrome of GEFS+ (generalized epilepsy with febrile seizures plus). Here, we generated *Scn1a*-targeted rats carrying a missense mutation (N1417H) in the third pore region of the sodium channel by gene-driven ENU (*N*-ethyl-*N*-nitrosourea) mutagenesis. Despite their normal appearance under ordinary circumstances, *Scn1a* mutant rats exhibited remarkably high susceptibility to hyperthermia-induced seizures, which involve generalized clonic and/or tonic–clonic convulsions with paroxysmal epileptiform discharges. Whole-cell patch-clamp recordings from HEK cells expressing N1417H mutant channels and from hippocampal GABAergic interneurons of N1417H mutant rats revealed a significant shift of the inactivation curve in the hyperpolarizing direction. In addition, clamp recordings clearly showed the reduction in action potential amplitude in the hippocampal interneurons of these rats. These findings suggest that a missense mutation (N1417H) of the $Na_v1.1$ channel confers susceptibility to FS and the impaired biophysical properties of inhibitory GABAergic neurons underlie one of the mechanisms of FS.

Introduction

Febrile seizures (FSs) are the most common type of convulsive events in childhood between 6 months and 6 years of age, affecting 2–5% of children worldwide. Most FSs are apparently benign (categorized as simple), but one-third are complex with a prolonged duration (>15 min) and are associated with a risk of subsequent epilepsy. Essentially, any illness that leads to an increase in body temperature, such as upper respiratory infection, pneumonia, and influenza, and even bathing, can lead to FS (Fukuda et al., 1997). Several familial studies and twin studies have indicated that genetic predisposition may contribute significantly to the etiology of FS, and recent genetic studies have shown that at least nine loci are responsible for FS (Nakayama, 2009).

Voltage-gated sodium channels are critical for the initiation and propagation of action potentials in neurons. Mutations in the human $Na_v1.1$ channel gene SCN1A have been reported in >200 cases, ranging in severity from the comparatively mild disorder of generalized epilepsy with febrile seizures plus (GEFS+) to the epileptic encephalopathy of severe myoclonic epilepsy in infancy (SMEI). In GEFS+, FS persists beyond the age of 6 and may be accompanied by various other seizure types, including tonic–clonic, absence, and myoclonic seizures (Scheffer and Berkovic, 1997). SMEI, also known as Dravet's syndrome, is a severe epileptic encephalopathy, characterized by onset of FS by age 1 and the emergence between ages 1 and 4 of other seizure types, including myoclonic, focal, absence, and atonic seizures, along with developmental decline (Dravet et al., 2005). All SCN1A mutations responsible for GEFS+ have been found to be missense mutations, whereas one-half of the mutations in SMEI are truncated and presumably loss of function, and the remaining one-half are missense mutations (Meisler and Kearney, 2005; Mulley et al., 2005; Lossin, 2009).

Animal models of FS have contributed to fundamental understanding of the underlying mechanisms of FS (Holtzman et al.,

Received July 8, 2009; revised March 2, 2010; accepted March 10, 2010.

This work was supported in part by a research grant from the Japan Epilepsy Research Foundation; Ministry of Education, Culture, Sports, Science and Technology Grant-in-Aid for Scientific Research 16200029; and Industrial Technology Research Grant Program in 2008 from New Energy and the Industrial Technology Development Organization of Japan. We thank T. Kuramoto and B. Voigt for critical discussion and movie preparation, and F. Tagami, Y. Kunihiro, S. Tokuda, N. Sofue, and S. Nakanishi for experimental assistance.

Correspondence should be addressed to Tomoji Mashimo, Institute of Laboratory Animals, Kyoto University Graduate School of Medicine, Yoshidakonoe-cho, Sakyo-ku, Kyoto 606-8501, Japan. E-mail: tmashimo@anim.med.kyoto-u.ac.jp.

DOI:10.1523/JNEUROSCI.3360-09.2010

 0270-6474/10/305744-10$15.00/0

1981). In a well established model, exposing rat pups to hyperthermia provokes seizures with elevating body temperature to a level comparable with human fever (Chen et al., 1999; Schuchmann et al., 2006). Mice heterozygous for the knock-out allele at the *Scn1a* locus have been recently reported as a potential animal model of SMEI (Yu et al., 2006; Ogiwara et al., 2007): these mice mainly develop epileptic seizures, whereas homozygous mice show ataxia and die on postnatal day 15. Very recently, hyperthermia stimuli of the heterozygous mice demonstrated seizure susceptibility before the spontaneous seizure developed (Oakley et al., 2009). Although these observations can explain the epileptic phenotype of SMEI, the relationship between sodium channel functions and the onset of FS is still poorly understood. It is likely that the best animal models for FS would not result from a null allele of the *Scn1a*, but rather from an allele with a missense mutation.

In this study, using gene-driven *N*-ethyl-*N*-nitrosourea (ENU) mutagenesis, we generated *Scn1a*-targeted rats carrying a missense mutation (N1417H) in the third pore region of the sodium channel. *Scn1a* mutant rats exhibited markedly high susceptibility to experimental FS, thus designated as hyperthermia-induced seizure-susceptible (Hiss) rats. The N1417H mutation of *Scn1a* resulted in abnormal inactivation of $Na_v1.1$ channels at hyperpolarized membrane potentials. This mutation in the rat allows additional investigations to understand the etiology of FS and/or associated epilepsy.

Materials and Methods

All animal care and experiments conformed to the Guidelines for Animal Experiments at Kyoto University and were approved by the Animal Research Committee of Kyoto University.

ENU mutagenesis in rats. ENU mutagenesis procedures in rats were previously described (Mashimo et al., 2008). Briefly, we administered two doses of 40 mg/kg ENU by intraperitoneal injection to F344/NSlc male rats at 9 and 10 weeks of age. Ten weeks after the second ENU treatment, males were mated with F344/NSlc females to generate 1735 G_1 male offspring, whose genomic DNA and sperm were cryopreserved in the Kyoto University Rat Mutant Archive (KURMA) (Mashimo et al., 2008). The sperm archive KURMA has been deposited in the National Bio Resource Project for the Rat in Japan (www.anim.med.kyoto-u.ac.jp/nbr) and is open to any interested researcher worldwide. For sperm cryopreservation, a clump of spermatozoa were taken from the caudal epididymides of 10-week-old rats and dispersed in 1 ml of mR1ECM medium (Hirabayashi et al., 2002). The sperm suspension was then sonicated for 10 s with an ultrasonic cell disruptor (UR-20P; Tomy Seiko) and transferred into 1.0 ml microtubes (Nalge Nunc International). The sperm tubes were frozen in liquid nitrogen vapor and finally stored in liquid nitrogen.

Screening protocols with MuT-POWER on the KURMA were described previously (Mashimo et al., 2008). Eight independent G_1 DNA samples were pooled for subsequent PCRs. Primers were designed to amplify the exonic region of the rat *Scn1a* gene from ~50 bp flanking each intron (supplemental Table 1, available at www.jneurosci.org as supplemental material). PCRs were performed in a total volume of 15 μl under the following conditions: 94°C for 3 min for 1 cycle, 94°C for 30 s, 60°C for 30 s, and 72°C for 1 min for 35 cycles. The final reaction conditions were 100 ng of genomic DNA, 200 μM each dNTP, 1.0 mM $MgCl_2$, 0.66 μM each primer, and 0.4 U of TaqDNA polymerase (Invitrogen). The Mu transposition reactions were previously described (Yanagihara and Mizuuchi, 2002). The Mu transpososome mixture was prepared by mixing 300 nM MuA transposase, 100 nM labeled Mu-end DNA, and 25 mM HEPES, pH 7.6, 15% (v/v) glycerol, 15% DMSO, 10 mM 3-[(3-cholamidopropyl)dimethylammonio]-1-propanesulfonate (CHAPS), and 156 mM NaCl. Reactions were performed at 30°C for 1 h. The mixture was then split and mixed with PCR products and $MgCl_2$ activation buffer. The final Mu transposition reaction mixture contained 33 nM labeled Mu-end DNA, 100 nM MuA transposase, PCR products, 25 mM HEPES, pH 7.6, 15% (v/v) glycerol, 10% DMSO, 10 mM CHAPS, 10 mM $MgCl_2$, and 300 mM NaCl. Reactions were performed at 20°C for 5 min. The reaction mixture was then purified by CleanSEQ (Beckman Coulter) to remove dye-labeled oligos, followed by automatic electrophoresis on a 16-capillary 3100 DNA Sequencer (Applied Biosystems). When positive peaks were detected in the eight pooled samples by MuT-POWER screening, individual sequences of the eight independent samples were determined. The sequencing reactions were performed with BigDye terminator, version 3.1, cycle sequencing mix, followed by the standard protocol for the Applied Biosystems 3100 DNA Sequencer.

In the intracytoplasmic sperm injection (ICSI) procedure, sperm heads were injected into denuded oocytes at ambient temperature (23 ± 2°C) using a piezo impact-driving unit (PMM-150FU; Prime Tech) with a pulse controller (PMAS-CT150; Prime Tech). ICSI oocytes were cultured in 60 μl microdrops of mR1ECM medium at 37°C under mineral oil in 5% CO_2 in air. All nondegenerating one-cell oocytes and evenly cleaved two-cell oocytes at 23–25 h after ICSI were transferred into the oviductal ampullae of recipient Wistar/ST rats that had been previously mated with vasectomized males. Embryo transfers were performed on the day when the vaginal plug was detected (defined as day 1).

To eliminate mutations that might have been generated by ENU in other chromosomal regions of the *Scn1a* locus, more than five backcross generations were performed against the F344/NSlc inbred background. Heterozygous carriers were then intercrossed to produce homozygous individuals. The mean mutation frequency was ~1 in 4.0 million base pairs (Mashimo et al., 2008). Although the chance for the occurrence of a very tightly linked mutation with a phenotypic effect is very small, this possibility should be taken into account for the experimental design and interpretation of the results. We compared littermates to validate the effect of the observed mutation and to minimize the possibility of the before-mentioned circumstances.

Pentylenetetrazol- and hyperthermia-induced seizures. Pentylenetetrazol (PTZ) (Sigma-Aldrich) dissolved in saline was injected into the tail vein at three doses (10, 20, and 30 mg/kg) to 10- to 12-week-old male rats. The epileptic (ED_{50}) and lethal (LD_{50}) dose of PTZ, which induced seizures and associated death, respectively, in 50% of animals, was calculated by probit analysis.

Although exposing rat pups to a stream of hot air from a hair dryer has been a widely used model of experimental febrile seizures, we used hot water bathing since it can induce seizures in rats for a wider range of ages (1–10 weeks). Hot water-induced seizures were described by Klauenberg and Sparber (1984). A 30 × 60 × 60 tank contained 15-cm-deep 45°C water, whose temperature was controlled by a heater. The rats were placed in hot water for a maximum of 5 min or until a seizure occurred. The rectal temperature of rats was measured before and immediately after onset of the seizure with a probe inserted into the rectum (BAT-12; Physitemp). Diazepam (Wako) dissolved in 40% polyethyleneglycol solution (0.5 mg/kg) was administered intraperitoneally to the animals 30 min before the experiment.

For EEG recording, rats of 4 weeks of age were anesthetized with an intraperitoneal injection of pentobarbital (40 mg/kg, i.p.). With the animal's head fixed in a stereotaxic instrument (David Kopf), screw electrodes were placed on the right or left frontal and occipital cortex. A reference electrode was placed on the frontal cranium. The electrodes were then connected to a miniature plug and fixed to the skull with dental cement. After a 1 week recovery period, animals with implanted electrodes were subjected to the hyperthermia-induced seizure (HIS) experiments described above. Cortical EEGs were recorded, under free-moving conditions, with an amplifier (MEG-6108; Nihon Kohden) and a recorder (RTA-1100; Nihon Kohden), and the signals were stored in a computer (ML845; PowerLab) for later analysis. Behavioral changes were simultaneously observed.

Expression analysis of Scn1a. Whole brains were isolated from F344/NSlc and Hiss rats at postnatal ages 1, 2, 3, 5, and 10 weeks ($n = 3$ each). Total RNA samples were extracted by Isogen reagent (Nippon Gene). First-strand cDNA was synthesized from 5 μg of DNase-treated total RNA using oligo-dT_{12-18} primer and SuperScript II reverse transcriptase (Invitrogen). Quantitative PCR was performed using SYBR Premix Ex Taq polymerase and a Thermal Cycler Dice Real-Time System TP800 (Takara). The following

primers were used to specifically amplify respective genes: rat *Scn1a* gene, 5′-TTGCTTTGGAATCACGCATCTC-3′ and 5′-GAGGTGCCTATGGTCTGCTTCTGTA-3′; rat *Scn3a* gene, 5′-CGATGCAATTCACCCTGGAAG-3′ and 5′-GTGGCGACGCTGAAGTTCTC-3′. The cycling conditions comprised 10 s polymerase activation at 95°C and 30 cycles at 95°C for 5 s and 60°C for 30 s. The data acquisition step was performed at 60°C, and final melting curve analysis was used to ensure amplification of a single product. This experiment was performed three times independently, and each RNA sample was analyzed at least in duplicate. All relative quantification of gene expression with real-time PCR data was performed using the comparative threshold (Ct) cycle method. The Ct values of target genes were normalized to the levels of GAPDH as an endogenous control at each time point.

Western blotting was performed using the cell lysate from the hippocampus using standard methods. Signals were detected with antibodies against rat $Na_v1.1$ (AB5204; Millipore Bioscience Research Reagents) and β-actin (AC-40; Sigma-Aldrich).

Electrophysiological recordings of heterologously expressed recombinant SCN1A. Full-length human SCN1A ($Na_v1.1$) cDNA was provided by Dr. Al George (Vanderbilt University, Nashville, TN). The N1417H mutation was constructed by PCR-based site-directed mutagenesis. The N1417H fragment was digested with BglII and SalI, and then replaced the corresponding restriction fragment in the pCMVscript-SCN1A wild type (WT). The open reading frame of every construct was completely sequenced before use to exclude polymerase errors and rearrangements. Recombinant SCN1A-WT and N1417H were heterologously coexpressed with human β1 and β2 accessory subunits (generous gifts from Dr. Al George) in human embryonic kidney (HEK)-293 cells. Whole-cell voltage-clamp recordings were performed to characterize the functional properties of WT-SCN1A and N1417H. HEK-293 cells were grown in DMEM supplemented with 10% (v/v) fetal bovine serum (Atlanta Biologicals), 2 mM L-glutamine, and penicillin–streptomycin (50 U/ml and 50 μg/ml, respectively) in a humidified 5% CO_2 atmosphere at 37°C. Expression of SCN1A, β1, and β2 was achieved by transient plasmid transfection using QIAGEN Superfect reagent. Sodium channel currents were recorded from transfected HEK293 cells at room temperature using Axopatch 200B amplifiers (Molecular Devices). Pipette resistance was between 1.3 and 2.0 MΩ. The pipette solution consisted of the following (in mM): 110 CsF, 10 NaF, 20 CsCl, 2 EGTA, 10 HEPES, with a pH of 7.35 and osmolarity of 310 mOsmol/kg. The bath solution consisted of the following (in mM): 145 NaCl, 4 KCl, 1.8 $CaCl_2$, 1 $MgCl_2$, 10 HEPES, with a pH of 7.35 and osmolarity of 310 mOsmol/kg. Cells were allowed to stabilize for 10 min after establishing the whole-cell configuration before currents were recorded. Whole-cell capacitance and access resistance were determined by integrating capacitive transients in response to voltage steps from −120 to −110 mV filtered at 5 kHz. Series resistance (2 ± 0.1 MΩ) was compensated 87–95% to assure that the command potential was reached within microseconds with a voltage error <3 mV. Leak currents were subtracted using the P/4 procedure. All data were low-pass Bessel filtered at 5 kHz and digitized at 10–50 kHz. Specific voltage-clamp protocols assessing channel activation, steady-state inactivation, and recovery from fast inactivation were used. Representations of all voltage protocols are included as insets in the figures. Persistent current was evaluated during the final 10 ms of a 100 ms depolarization to −10 mV and expressed as a percentage of peak current after digital subtraction of currents recorded in the presence and absence of 10 μM tetrodotoxin (TTX) (Sigma-Aldrich). Results are presented as the mean ± SEM, and statistical comparisons were made in reference to WT-SCN1A using the unpaired Student's *t* test. Data analysis was performed by using Clampfit 8.2 (Molecular Devices) and OriginPro 7.0 (OriginLab) software.

Whole-cell recording in dissociated hippocampal neurons. Hippocampal pyramidal cells and bipolar cells were freshly dissociated from 11- to 16-d-old F344/NSlc and Hiss ($Scn1a^{Kyo811/Kyo811}$) rats. Coronal slices (350 μm thick) of the hippocampus were prepared using a microslicer (Linear Slice PRO7; Dosaka). After preincubation in Krebs' solution for 40 min at 31°C, the slices were digested: first in Krebs' solution containing 0.017% Pronase (Calbiochem/Novabiochem) for 20 min at 31°C, and then in solution containing 0.017% thermolysin (type X; Sigma-Aldrich) for 20 min at 31°C. The Krebs' solution used for preincubation and digestion contained the following (in mM): 124 NaCl, 5 KCl, 1.2 KH_2PO_4, 2.4 $CaCl_2$, 1.3 $MgSO_4$, 24 $NaHCO_3$, and 10 glucose. The solution was continuously oxygenated with 95% O_2 and 5% CO_2. CA1 regions at the pyramidal layer or at a distance of 50–200 μm from the pyramidal layer were punched out and dissociated mechanically using fine glass pipettes with a tip diameter of 100–200 μm. Dissociated cells settled on tissue culture dishes (Primaria no. 3801; BD Biosciences) within 30 min. Hippocampal bipolar neurons were identified by their bipolar shape.

Electrophysiological measurements were performed on hippocampal pyramidal cells and bipolar cells. Currents were recorded at room temperature (22–25°C) using the whole-cell mode of the patch-clamp technique with an EPC-9 patch-clamp amplifier (HEKA). Patch pipettes were made from borosilicate glass capillaries (1.5 mm outer diameter; Hilgenberg) using a model P-97 Flaming-Brown micropipette puller (Sutter Instrument). Pipette resistance ranged from 2 to 4 MΩ when filled with the pipette solutions described below. Series resistance was electronically compensated to >50%, and both the leakage and remaining capacitance were subtracted by the −P/5 method. Currents were sampled at 100 kHz after low-pass filtering at 10 kHz. Stimulation and data acquisition were performed using the PULSE program (version 7.5; HEKA Elektronik). Sodium currents were recorded in an external solution that contained the following (in mM): 19.1 NaCl, 19.1 TEA-Cl (tetraethylammonium chloride), 0.95 $BaCl_2$, 1.90 $MgCl_2$, 52.4 CsCl, 0.1 $CdCl_2$, 0.95 $CaCl_2$, 9.52 HEPES, 117 glucose, pH adjusted to 7.35 with NaOH. The pipette solution contained the following (in mM): 157 *N*-methyl-D-glucamine (NMDG), 126 HCl, 0.90 NaCl, 3.60 $MgCl_2$, 9.01 EGTA, 1.80 $ATPNa_2$, 9.01 HEPES, 4.50 creatine-phosphate, pH adjusted to 7.2 with NMDG. Conductance–voltage (*g–V*) relationships were calculated from current–voltage (*I–V*) relationships according to $g = I_{Na}/(V - E_{Na})$, where I_{Na} represents the peak sodium current measured at potential *V*, and E_{Na} represents the equilibrium potential. Normalized activation and inactivation curves were fitted to Boltzmann relationships of the following form: $y = 1/(1 + \exp[(V_{0.5} - V)/k])$, where *y* is normalized g_{Na} or I_{Na}, *V* is the membrane potential, $V_{0.5}$ is the voltage of half-maximal activation, or inactivation, and *k* is the slope factor. Inactivation time constants were evaluated by fitting the current decay with single exponential function: $I = A \times \exp(-t/\tau) + C$, where *I* is the current, *A* is the current inactivated with time constants τ, and *C* is the noninactivating current.

Whole-cell voltage recordings were made at room temperature (22–25°C) using the current-clamp mode with an Axopatch 200B patch-clamp amplifier (Molecular Devices). Hippocampal pyramidal cells and bipolar cells were held at −80 mV, and their firing patterns were recorded in response to sustained depolarizations or hyperpolarizations (duration, 800 ms; increments, ±5 pA) (Yu et al., 2006). The intracellular solution contained the following (in mM): 135 potassium gluconate, 20 KCl, 2 $MgCl_2$, 2 $ATPNa_2$, 0.3 GTPNa, and 10 HEPES, 0.2 EGTA, pH adjusted to 7.3 with KOH. The extracellular solution contained the following (in mM): 140 NaCl, 5 KCl, 2 $CaCl_2$, 1 $MgCl_2$, 10 HEPES, and 10 glucose, pH adjusted to 7.4 with NaOH. The input–output relationship, action potential half-width, spike amplitude, and spike decrement were measured. The input–output relationship was defined as the dependence of the number of action potentials generated on the amplitude of current injection. Action potential half-width was defined as the width at half-maximum amplitude of the action potential. Spike decrement was calculated as percentage of last spike amplitude divided by first spike amplitude.

Statistical comparison between F344/NSlc and Hiss rats was performed by Student's *t* test ($^*p < 0.05$; $^{**}p < 0.01$; $^{***}p < 0.001$).

Results

Targeted mutations in the rat *Scn1a*

To generate a rat model carrying a mutation in the *Scn1a*, we used the chemical mutagen ENU and our recently developed strategy, combining a high-throughput screening assay making use of the Mu-transposition reaction (MuT-POWER) and ICSI to recover rare heterozygous mutations from our frozen sperm repository (Mashimo et al., 2008). Screening of 1735 G_1 samples by MuT-

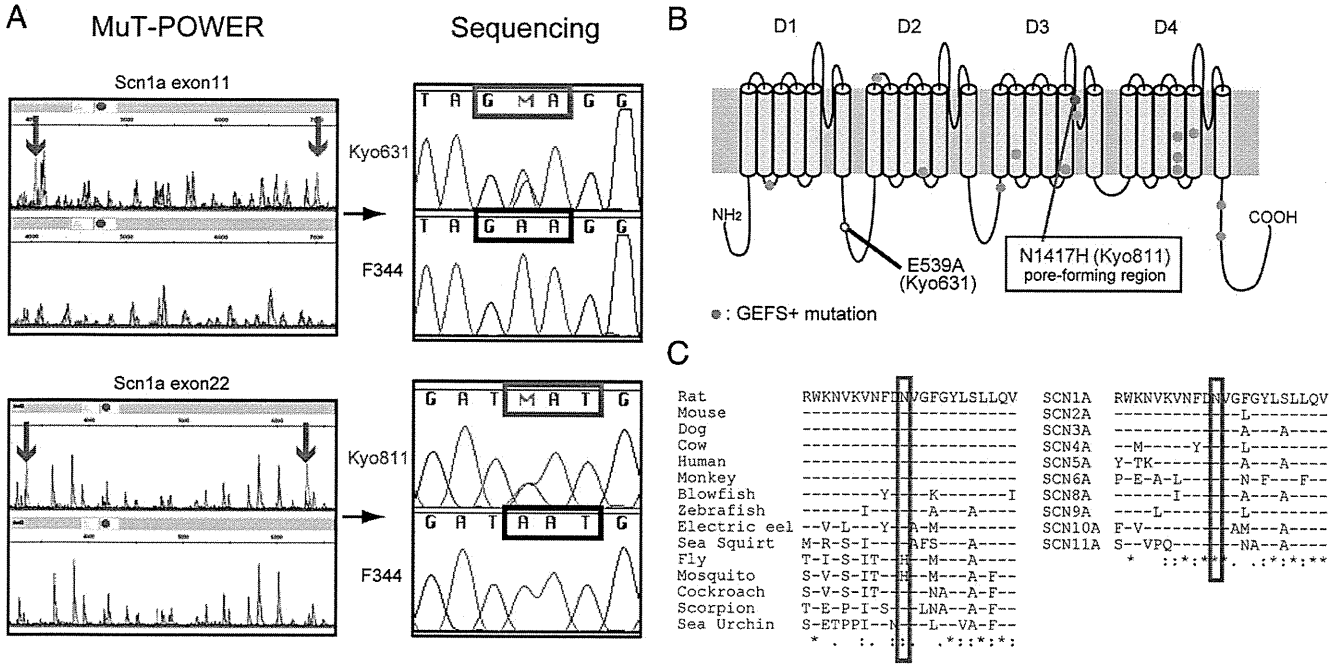

Figure 1. Identification of two mutations for the rat *Scn1a* gene ($Na_v1.1$) by MuT-POWER screening of G_1 rats. ***A***, Two positive peaks were detected with the primer sets amplifying exons 11 and 22 of the rat *Scn1a* gene. Both mutations were confirmed in individual Kyo631 and Kyo811 G_1 samples, respectively, by sequencing. Mutations appear as green peaks and are indicated with red arrows. Other overlapping green and blue peaks are background. ***B***, N1417H was located in the third pore region of the sodium channel. ***C***, N1417H is highly conserved among other species as well as in other genes encoding a sodium channel. Fly and mosquito have the same amino acid change of Kyo811, suggesting functional differences in channels from these species compared with vertebrates.

POWER for mutations at the rat locus orthologous to the human *SCN1A* gene, we were able to identify two mutations: Kyo631 and Kyo811 (Fig. 1*A*). Sequence analysis revealed that these two mutations were both single-nucleotide substitutions, A1616C and A4246C, resulting in amino acid changes, E539A and N1417H, respectively. The SIFT prediction (http://blocks.fhcrc.org/sift/SIFT.html) suggested that the N1417H substitution may markedly affect protein function. N1417H mutation is located in the pore region of the sodium channel in a domain that is highly conserved among other species as well as in other genes of the sodium channel family (Fig. 1*C*).

The recovery of two identified mutant rats, Kyo631 and Kyo811, from frozen sperm cells was achieved by ICSI, yielding 24 live rats, of which 6 and 5 rats, respectively, were confirmed heterozygous for the mutations by direct sequencing (supplemental Table 2, available at www.jneurosci.org as supplemental material). To eliminate mutations that might have been generated by ENU in other chromosomal regions of the *Scn1a* locus, more than five backcross generations were performed against the F344/NSlc inbred background. Heterozygous carriers were then intercrossed to produce homozygous individuals for both $Scn1a^{Kyo631}$ and $Scn1a^{Kyo811}$ alleles. Although the occurrence of a very tightly linked mutation with a phenotypic effect is very small, this possibility should be taken into account when designing the experiment and interpreting the results. We therefore compared littermates to validate the effect of the observed mutation. Both $Scn1a^{Kyo631}$ and $Scn1a^{Kyo811}$ strains appeared phenotypically normal without any obvious seizures. There were no apparent histological abnormalities in the brains of both rats. Since human GEFS+ patients exhibit various forms of clinically recognized seizures, including tonic–clonic, absence, and myoclonic seizures (Scheffer and Berkovic, 1997), we tested the sensitivity of *Scn1a* rats to seizures induced by the convulsant PTZ, a $GABA_A$ receptor–chloride channel complex blocker. Rats homozygous F344-$Scn1a^{Kyo811/Kyo811}$ showed much higher susceptibility to PTZ than F344/NSlc, F344-$Scn1a^{Kyo631/Kyo631}$, and heterozygous F344-$Scn1a^{Kyo811/+}$ (Fig. 2*A*; supplemental Table 3, available at www.jneurosci.org as supplemental material).

Susceptibility to HIS

The most common symptoms of GEFS+ are FS and FS plus, in which the seizures are triggered by hyperthermia and occur after 6 years of age (Scheffer and Berkovic, 1997; Baulac et al., 1999). To investigate whether *Scn1a* mutant rats are susceptible to thermal stimuli, we used a hot water bath to induce FS (Klauenberg and Sparber, 1984). F344/NSlc and F344-$Scn1a^{Kyo631/Kyo631}$ rats at 5 weeks of age showed no seizures when exposed to 45°C hot water for 5 min, whereas all homozygous F344-$Scn1a^{Kyo811/Kyo811}$ rats ($n = 11$) exhibited clonic seizures with an average latency of 3.5 ± 0.6 min after immersion in water (Fig. 2*B*). Two of 11 $Scn1a^{Kyo811/+}$ heterozygous rats showed clonic seizures with a latency of 4.7 ± 0.4 min. Rectal temperature of the homozygous rats at seizure induction (43.3 ± 0.3°C) was significantly lower than that of heterozygous rats (44.2 ± 0.7°C; $p < 0.007$). We considered that the brain temperature could be lower than the rectal temperature that was measured when inducing the seizures, since the head of each rat was not submerged in the heated bath. Wild, heterozygous, and homozygous rats showed no difference for a normal rectal temperature of 37.9–38.3°C. Immersing these rats in 37–40°C water did not evoke seizures.

The convulsive seizures of homozygous rats persisted even after removal from the water bath with an average duration of 1.8 ± 0.7 min with several recurrences (Fig. 2*B*). These intermittent seizures typically consisted of tonic flexion, clonic convulsion, wet dog shake, myoclonic jerks of the limbs, straub tail, and oral automatisms (supplemental Video 1, avail-

able at www.jneurosci.org as supplemental material). Cortical EEG recording indicated complete correlation in the occurrence between behavioral seizures and paroxysmal epileptiform discharges (Fig. 2*C*). These HISs were abolished ($n = 7$) by pretreatment of animals with diazepam (0.5 mg/kg, i.p.) (Fig. 2*B*), which is usually used as efficient treatment for FS in humans. These results indicate that the N1417H mutation within the pore region of *Scn1a* significantly increases susceptibility to experimental FS; therefore, we designated these hyperthermia-induced seizure-susceptible rats as "Hiss" rats.

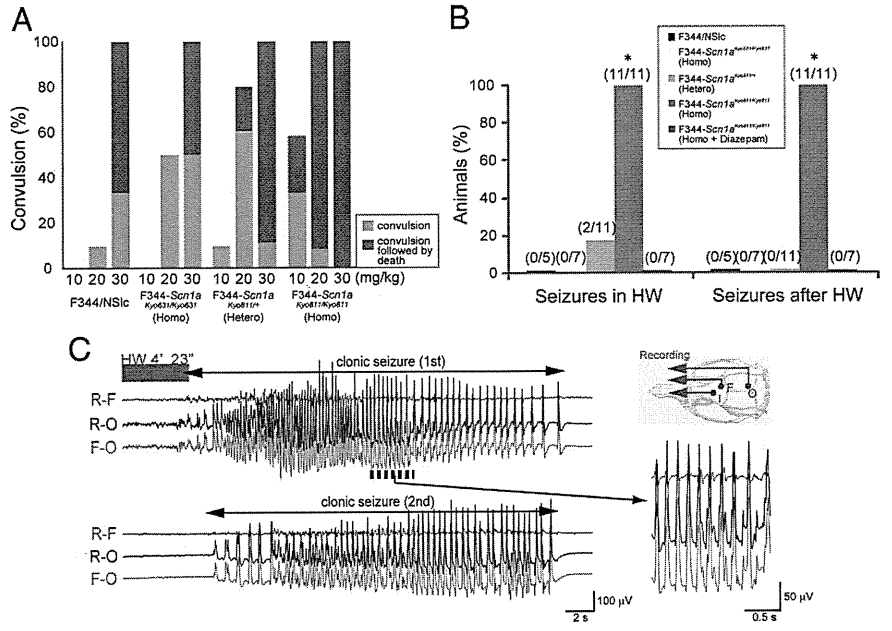

Figure 2. Susceptibility of *Scn1a* rats to PTZ and hyperthermia stimuli. ***A***, All strains exhibited dose-dependent PTZ-induced seizures, but susceptibility was increased slightly in heterozygous $Scn1a^{Kyo811/+}$ rats and significantly in homozygous $Scn1a^{Kyo811/Kyo811}$. The numbers of rats are described in supplemental Table 3 (available at www.jneurosci.org as supplemental material). ***B***, Quantitative analysis of the number of rats developing clonic seizures induced by hyperthermia in hot water (left) and extended convulsive seizures after taking them out of the water (right). The numbers of rats are indicated in parentheses. $*p < 0.01$. ***C***, Typical epileptic discharges during convulsion induced by hyperthermia (red bar) in the temporal cortex of homozygous rats at 5 weeks of age during clonic convulsion. The clonic convulsive seizures of homozygous rats extended after taking them out of the water with a few recurrences. In some homozygous rats, transient tonic convulsions were observed during clonic seizures. The insets show generalized cortical seizures on an expanded scale. F, Frontal cortex; O, occipital cortex; I, indifferent electrode.

Age-dependent susceptibility to HIS

In rodent models of FS, postnatal day 8 (P8) to P14 rats are most susceptible to HIS (Chen et al., 1999; Schuchmann et al., 2006). To clarify the relationship between *Scn1a* expression and susceptibility to HIS, we monitored the expression level of *Scn1a* and hot water-induced seizures at 1–10 weeks of age (Fig. 3; supplemental Table 4, available at www.jneurosci.org as supplemental material). Throughout the entire course of the experiments, the expression levels of *Scn1a* in the brain were similar between Hiss ($Scn1a^{Kyo811/Kyo811}$) and control F344/NSlc rats. At 1 and 2 weeks of age, *Scn1a* expression was very low (Fig. 3*A*,*B*), and the immersion of rats into 45°C water led to convulsive seizures in both F344/NSlc and Hiss rats (Fig. 3*C*). Seizures in such infantile rats, consisting of oral automatisms, myoclonic jerks of the limbs, and clonic convulsion, are generally milder than those seen in adult rats, and no sustained seizures were observed after removal from the water bath. No significant difference was observed between the two strains for apparent behavioral seizures and in the threshold temperature of seizure induction (supplemental Table 4, available at www.jneurosci.org as supplemental material).

At 3–5 weeks of age, *Scn1a* expression markedly increased and peaked at 5 weeks of age (Fig. 3*A*,*B*) in agreement with previous reports (Beckh et al., 1989; Gong et al., 1999). Susceptibility to HIS decreased with age and inversely with the increased expression of *Scn1a* in F344/NSlc rats (Fig. 3*A*,*B*), whereas the susceptibility remained in Hiss rats even at 10 weeks of age (Fig. 3*C*). In Hiss rats, sustained seizures were observed at 3, 5, and 10 weeks of age. Rectal temperature at seizure induction in Hiss rats was significantly lower than in control F344/NSlc rats (supplemental Table 4, available at www.jneurosci.org as supplemental material).

Electrophysiological properties of the N1417H channel

To investigate how the N1417H missense mutation affects neuronal activities, we examined the electrophysiological properties of the N1417H mutation using a heterologous expression system in human HEK293 cells (Lossin et al., 2002; Ohmori et al., 2006). Cells expressing the N1417H mutant channels exhibited a voltage-dependent inward current that resembled cells transfected with WT channels (Fig. 4*A*). Inactivation proceeded in a rapid biexponential manner, with no apparent difference between WT and N1417H (Fig. 4*B*). N1417H channels showed no difference in current density and voltage dependence channel activation compared with WT (Fig. 4*C*,*D*); however, N1417H exhibited a significant hyperpolarizing shift in half-maximal steady-state inactivation (Fig. 4*E*; supplemental Table 5, available at www.jneurosci.org as supplemental material). Moreover, recovery from fast inactivation was significantly slower in N1417H-expressing cells ($p < 0.05$) (Fig. 4*F*).

In previous reports, increased persistent sodium currents were observed in epilepsy-associated *Scn1a* mutant channels (Lossin et al., 2002; Meisler and Kearney, 2005; Stafstrom, 2007). Figure 4*G* illustrates representative, tetrodotoxin-subtracted current traces for WT-SCN1A and N1417H in response to a 100 ms voltage step to −10 mV from a holding potential of −120 mV. Cells expressing N1417H exhibited a significantly greater persistent current expressed as a percentage of peak current ($0.88 \pm 0.17\%$; $n = 11$) compared with WT-SCN1A ($0.38 \pm 0.10\%$; $n = 7$; $p < 0.05$) (Fig. 4*H*).

Sodium channel properties in hippocampal neurons

To access functional properties in native N1417H channels, we examined whole-cell sodium currents in hippocampal pyramidal cells (glutamatergic neurons) and bipolar cells (GABAergic interneurons) dissociated from 12- to 16-d-old F344/NSlc and Hiss rats ($Scn1a^{Kyo811}/Scn1a^{Kyo811}$). Whole-cell sodium currents recorded in pyramidal cells from F344/NSlc and Hiss rats were similar in current density, voltage dependence of activation, and voltage dependence of inactivation (supplemental Fig. 1, Table 6, available at www.jneurosci.org as supplemental material). In bipolar cells, the mean current amplitudes, capacitance, and densities were not significantly different between F344/NSlc and Hiss

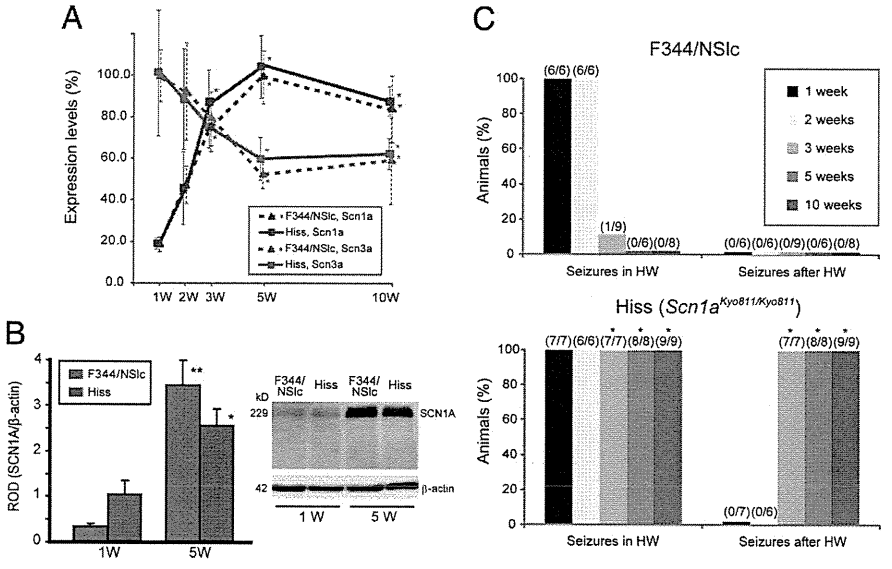

Figure 3. Developmental changes in *Scn1a* expression and susceptibility to hyperthermia-induced seizures. ***A***, *Scn1a* (red) and *Scn3a* (blue) mRNA quantification was expressed as a percentage of the maximum level, at different postnatal ages, 1–10 weeks, in the brain of F344/NSlc (triangle) and Hiss (rectangle) rats. Error bars indicate mean ± SE. $*p < 0.05$ for each age versus 1 week by ANOVA. ***B***, $Na_v1.1$ protein levels in the hippocampus of F344/NSlc (blue) and Hiss (red) rats at 1 and 5 weeks of age. The expression level was normalized against β-actin. $*p < 0.05$ and $**p < 0.01$ for 1 week versus 5 weeks by Student's *t* test. ***C***, Quantitative analysis of the number of rats developing clonic seizures induced by hyperthermia in hot water (left) and extended convulsive seizures after taking them out of the water (right), at different postnatal ages 1–10 weeks, for F344/NSlc (top) and Hiss (bottom) rats. The numbers of rats are indicated in parentheses. $*p < 0.01$ versus F344/NSlc.

rats (Fig. 5*A–C*). Voltage dependence of activation was not different between F344/NSlc and Hiss rats, whereas inactivation showed different voltage dependence, in which the curve significantly shifted in the hyperpolarizing direction in Hiss rats (Fig. 5*D,E*; supplemental Table 7, available at www.jneurosci.org as supplemental material). The mean inactivation time constants were not different between F344/NSlc and Hiss rats (Fig. 5*F*). Persistent sodium currents, evaluated during the final 10 ms of a 100 ms depolarization to −30 mV, were significantly increased in hippocampal bipolar cells of Hiss rats ($p < 0.05$) (Fig. 5*G,H*).

We examined how these abnormal properties of the sodium channels affected neuronal firing patterns. We recorded the action potentials that originated from dissociated hippocampal pyramidal neurons and bipolar neurons in response to a series of current injections and determined the input–output relationship. The number of action potentials and their firing patterns were similar for pyramidal neurons from F344/NSlc and Hiss rats (supplemental Fig. 2, available at www.jneurosci.org as supplemental material). The number of action potentials for bipolar cells was similar, but was slightly reduced for Hiss rats with increasing injected current (Fig. 6*A,B*). At 95 pA injected current, the first and last spike amplitudes of the action potential were significantly reduced for Hiss rats (Fig. 6*C*). The width of their firing patterns was slightly broader at 95 pA injected current (Fig. 6*D*). These results indicate that interneuron excitability was slightly reduced in the hippocampus of the Hiss rat.

Discussion

Animal models of FS have been previously established. For these, convulsive activity is evoked by exposing rats to hyperthermia, which increases their body temperature to a level that is comparable with a human fever. Methods include using heated air (Holtzman et al., 1981; Chen et al., 1999; Schuchmann et al., 2006), jets of hot water that are applied to the head (Ullal et al., 1996), or through bathing in hot water (Klauenberg and Sparber, 1984). These models permitted fundamental discoveries about their underlying mechanisms and consequences for developing epilepsy. However, significant gaps in our knowledge remain regarding the role of genetic predispositions toward FS, which has often been observed in human families. In this study, by using the ENU mutagenesis approach, we generated *Scn1a*-targeted Hiss rats. The rats carried a N1417H missense mutation in the third pore region of the sodium channel, in which several mutations have been reported for SMEI and GEFS+ families (Sugawara et al., 2001; Lossin, 2009). Using this model, we found that the $Na_v1.1$ channel plays an important role in controlling experimental FS. To our knowledge, the Hiss rat is the first animal model of FS that combines experimental FS models, such as hyperthermia-induced seizures, with a genetic predisposition, a missense mutation in the $Na_v1.1$ gene.

FS in humans is clearly age dependent in children between 6 months and 6 years of age, whereas P8–P14 rats are most susceptible to experimental FS (Holtzman et al., 1981; Chen et al., 1999; Schuchmann et al., 2006). Although superimposing the developmental stages of the rodent brain onto those of the human brain is difficult, the P12–P13 rat seems to correspond to a full-term human neonate (Romijn et al., 1991). The transiently high susceptibility to experimental FS that is seen for rats can be expected to occur before birth for humans, when GABAergic inhibition is relatively immature. During the first two postnatal weeks for rats and most likely during the late prenatal and early postnatal period for humans, GABA promotes a paradoxical excitatory activity. This is attributable to a larger intracellular Cl^- concentration, which depolarizes neurons (Ben-Ari and Holmes, 2006). The shift from a depolarizing to hyperpolarizing Cl^- concentration simultaneously occurs at P14 for rats with a decrease in NKCC1 cotransporter expression. This facilitates Cl^- accumulation in neurons and increased KCC2 cotransporter expression, which extrudes intracellular Cl^- (Dzhala et al., 2005). The age-dependent expression patterns of NKCC1 and KCC2 are quite similar to those of *Scn3a* and *Scn1a*, respectively, which we observed in this study (Fig. 3). Moreover, the susceptibility of F344 rats to HIS disappeared after 3 weeks of age in parallel with *Scn1a* expression. However, the Hiss rats remained susceptible probably because of the impaired function of the mutated $Na_v1.1$ channel. Generally, human FS occurs suddenly and without any obvious symptoms, except for a rapid rise of fever usually within 24 h of fever onset. The Hiss rat displays a typical convulsive seizure when its body temperature reaches a certain threshold, with extended seizures occurring after being removed from hot water (supplemental Video 1, available at www.jneurosci.org as supplemental material). Human and rat FSs are effectively prevented by using anticonvulsants such as diazepam. Considering the behavioral similarity of the seizures and the neuronal developmental conditions in the brain, the Hiss rat is a useful animal model of human FS and FS+. It will therefore enable a better understanding of the etiology of FS and/or associated epilepsy.

GEFS+ is a familial epilepsy syndrome for which the majority of patients present with typical FS or FS+. In addition, patients can have afebrile seizures, including generalized tonic–clonic seizures, myoclonic seizures, atonic seizures, or myoclonic–astatic epilepsy (Scheffer and Berkovic, 1997). For Hiss rats, obvious spontaneous seizures are very rare. Only a few cases of typical tonic–clonic seizures have been observed for adults. The potential contribution of FS to temporal lobe epilepsy is a topic of interest (Baulac et al., 2004; Dubé et al., 2007; Sadleir and Scheffer, 2007). Prospective studies suggested that a history of long or complex FSs significantly increases the risk for epilepsy. However, the precise mechanisms that mediate early-life epileptogenesis remain unknown. Animal models of FS show that experimentally prolonged FS elicits long-lasting changes in neuronal function, which might lead to limbic epilepsy (Dubé et al., 2006). For Hiss rats, neither prolonged experimental FS nor repetitive FS between 3 and 5 weeks of age evoked obvious epileptic seizures in the adults. However, this should be investigated in better detail using more sophisticated equipment. For example, a systematic video-EEG monitoring system could be used to detect spontaneous seizures, which might rarely occur in the adults.

Hyperthermia does not encompass the spectrum of biological processes of FS. However, temperature influences numerous cellular processes, including the activities of several types of neuronal ion channels and the electrical activity of neurons. This could enhance the rate, magnitude, or synchrony of neuronal firing and lead to seizures (Hodgkin and Katz, 1949; Moser et al., 1993). This is supported by the observation that FS was induced for Japanese patients who bathed in hot water (Fukuda et al., 1997). Some authors have also reported a considerable coexistence of FS of 5–15% for family histories of patients who suffer from hot water epilepsy (Mani et al., 1974; Satishchandra, 2003). Evidence exists that hyperthermia per se triggers seizures *in vivo* (Chen et al., 1999; Schuchmann et al., 2006) and induces epileptiform activity *in vitro* (Wu et al., 2001). For one *in vivo* model, increased body temperature for rat pups leads to a pronounced increase in the respiration rate. This is followed by an increase in brain pH, which triggers ictal activity, also known as respiratory alkalosis (Schuchmann et al., 2006). It would be interesting to study whether the $Na_v1.1$ channel mutation influences the pH sensitivity of the brain,

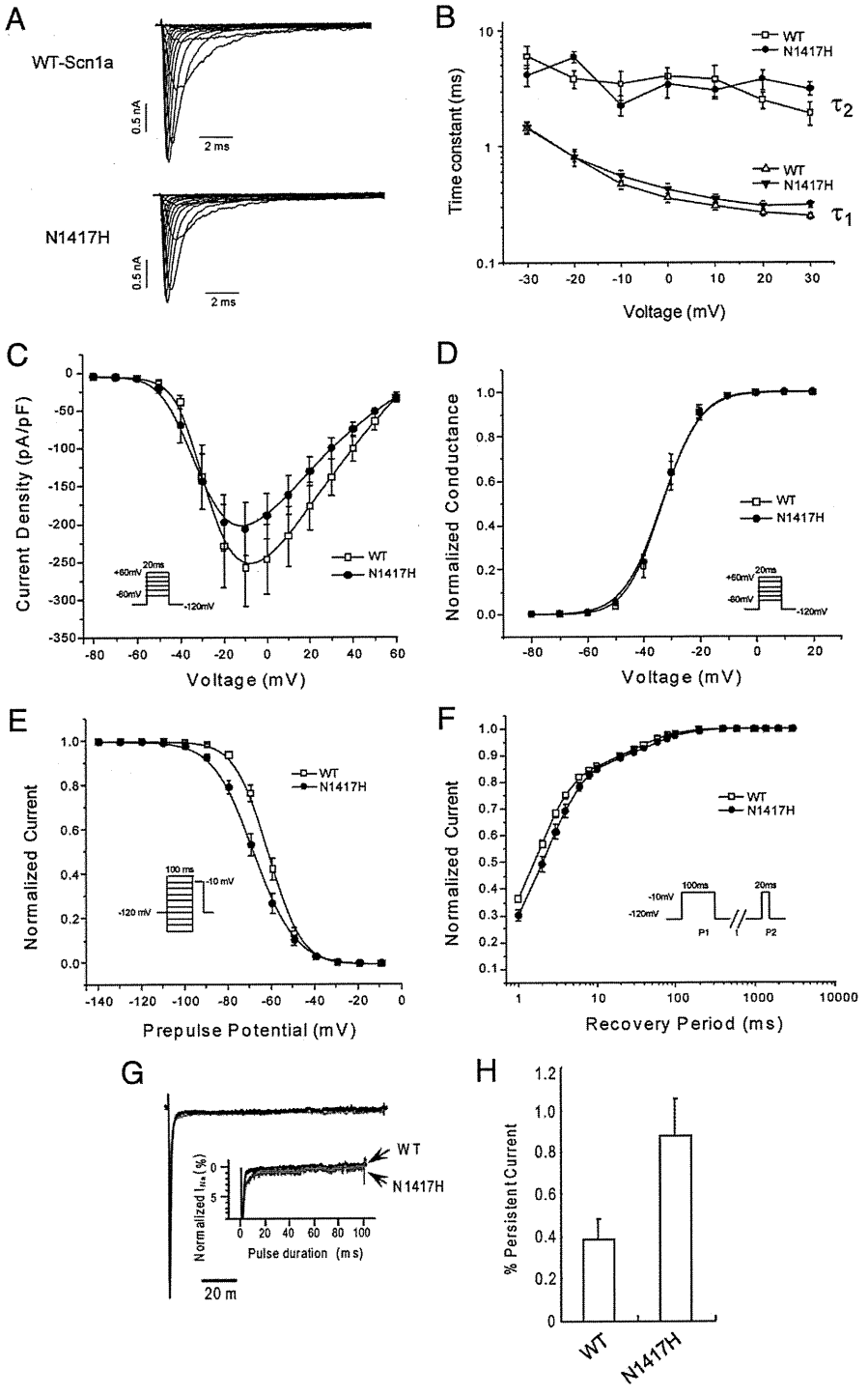

Figure 4. Sodium currents recorded from HEK293 cells expressing either WT-SCN1A or N1417H. ***A***, Representative whole-cell sodium currents. The currents were activated by voltage steps to between −80 and +60 mV in 20 mV increments from a holding potential of −120 mV. ***B***, Voltage dependence of fast inactivation time constants for WT-SCN1A and N1417H. Fast and slow time constants were plotted versus voltage. ***C***, Peak current density of whole-cell currents elicited by test pulses to various potentials and normalized to cell capacitance. WT, $n = 8$; N1417H, $n = 10$. ***D***, Voltage dependence of channel activation measured during voltage steps to between −80 and +20 mV from a holding potential of −120 mV. ***E***, Voltage dependence of fast inactivation measured at −10 mV in response to a 100 ms prepulse voltage step to between −140 and −10 mV from a holding potential of −120 mV. ***F***, Recovery from fast inactivation was evaluated using a two-pulse protocol, and the data were fitted with a two-exponential function. Time-dependent recovery from fast inactivation measured at −10 mV between 1 and 3000 ms immediately after a 100 ms prepulse voltage step to −10 mV from a holding potential of −120 mV. ***G***, Representative tetrodotoxin-subtracted whole-cell sodium currents recorded from HEK293 cells expressing WT-SCN1A and N1417H. Persistent current was measured in response to a 100 ms voltage step to −10 mV from a holding potential of −120 mV. Each current trace has been normalized to its peak sodium current. The inset shows an expanded *y*-axis scaled to emphasize the relative proportion of persistent current. ***H***, Quantification of persistent current as a percentage of peak current for WT ($n = 7$) and N1417H ($n = 7$). Error bars indicate mean ± SE.

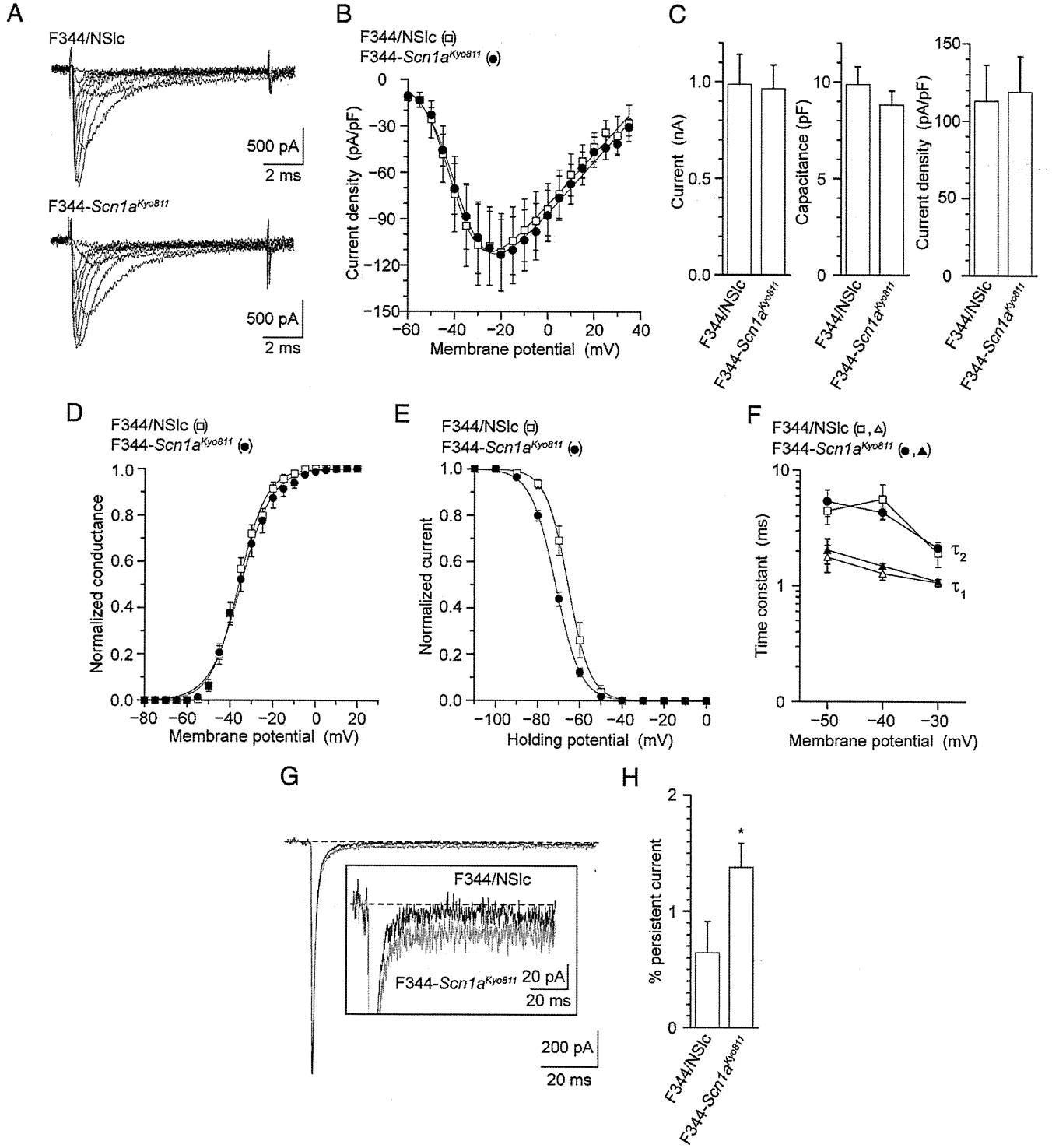

Figure 5. Comparison of sodium currents recorded in hippocampal bipolar neurons dissociated from F344/NSIc and Hiss rats. ***A***, Families of sodium currents evoked by 10 ms depolarizing pulses from −60 to 20 mV with 10 mV increments at a V_h of −100 mV in hippocampal bipolar neurons dissociated from F344/NSIc (top) and Hiss (bottom) rats. ***B***, *I–V* relationships for F344/NSIc (open squares; $n = 8$) and Hiss (filled circles; $n = 14$). ***C***, Comparison of peak current amplitudes (left), cell capacitances (middle), and current densities (right). Sodium currents elicited by a step pulse from a V_h of −100 to −20 mV are analyzed. Means ± SE are shown. ***D***, Voltage dependence of activation for F344/NSIc (open squares; $n = 8$) and Hiss (filled circles; $n = 14$). Half-maximal activation occurred at −37.4 ± 1.3 mV with a slope factor of 6.6 ± 0.3 for F344/NSIc and at −36.5 ± 1.8 mV with a slope factor of 6.6 ± 0.2 for Hiss. ***E***, Voltage dependence of inactivation for F344/NSIc (open squares; $n = 5$) and Hiss (filled circles; $n = 13$). Amplitudes of currents evoked by the test pulse to −20 mV after a 100 ms V_h prepulse to various membrane potentials between −110 and 0 mV were normalized to the current amplitude induced by the test pulse after a 100 ms V_h prepulse of −100 mV. The mean values were plotted as a function of potentials of 100 ms V_h prepulse and were fitted to the Boltzmann equation. Membrane potentials for half-maximal inactivation and slope factors were as follows: F344/NSIc, −65.6 ± 1.8 mV and −4.8 ± 0.3; Hiss, −71.5 ± 0.8 mV ($p < 0.05$) and −5.7 ± 0.2 ($p < 0.05$). ***F***, Inactivation time constants of hippocampal bipolar neurons from F344/NSIc (open symbols; $n = 21$) and Hiss (filled symbols; $n = 23$). Current decay was fitted by a sum of two exponential functions. The mean inactivation time constants for fast τ_1 (open triangles and filled triangles) and slow τ_2 (open squares and filled circles) were plotted as a function of test potentials from −50 to −30 mV. ***G***, Representative sodium current was evoked by 100 ms depolarization to −30 mV from V_h. TTX-sensitive currents were obtained by digital subtraction of sodium currents recorded before and after 1 μM TTX addition. The inset shows an expanded vertical scale to emphasize the relative proportion of the persistent current. ***H***, Persistent sodium currents in hippocampal bipolar neurons from F344/NSIc ($n = 17$) and Hiss ($n = 12$). Persistent current was evaluated during the final 10 ms of 100 ms depolarization to −30 mV. Error bars indicate mean ± SE if larger than symbols. *$p < 0.05$ versus F344/NSIc.

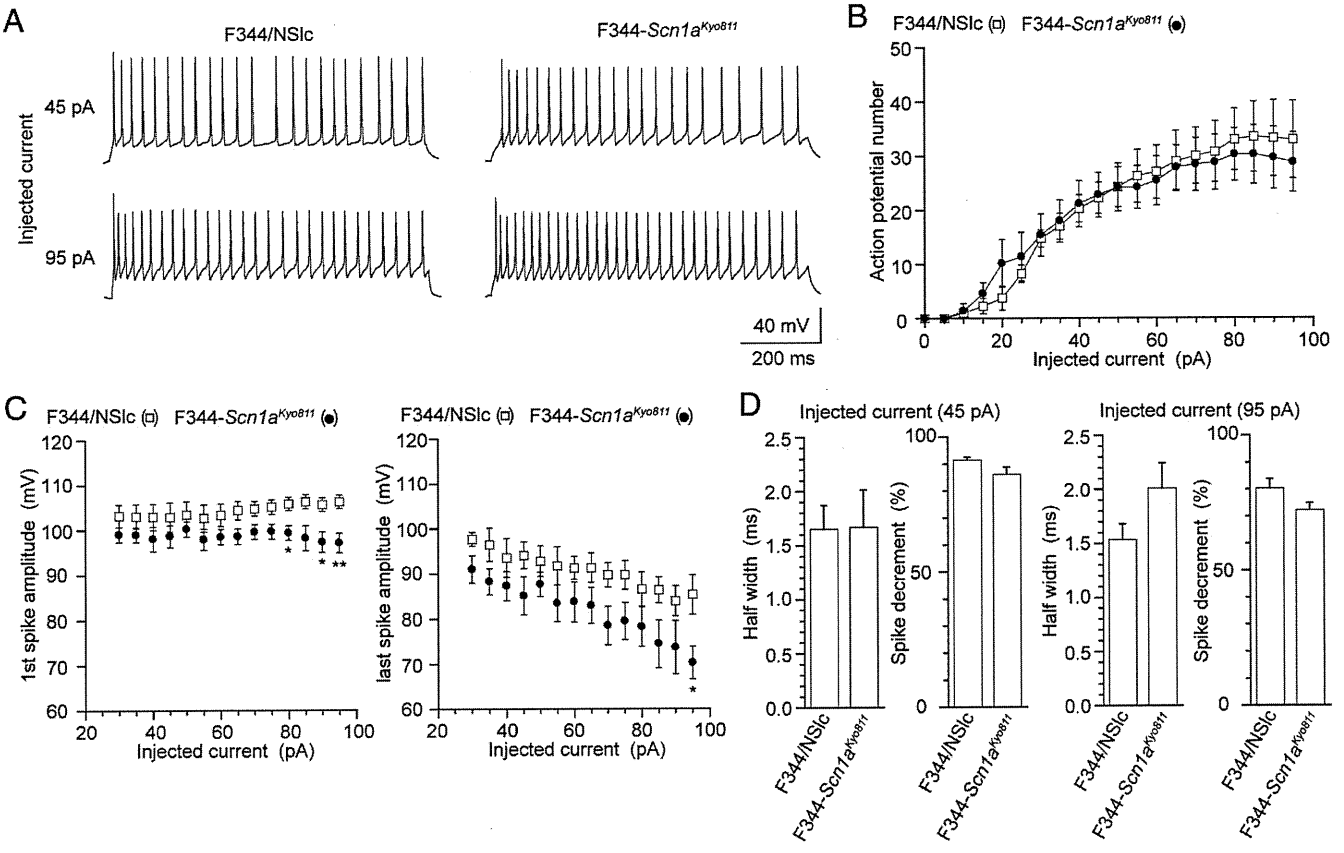

Figure 6. Depolarization-evoked firing activity of hippocampal bipolar neurons that have been dissociated from F344/NSIc and Hiss rats. ***A***, Representative sets of action potential traces recorded for F344/NSIc and Hiss hippocampal bipolar neurons during 800 ms injections of 45 pA (top) and 95 pA of current (bottom), for a membrane potential of −80 mV. ***B***, Input–output relationship for the number of action potentials elicited versus the injected current for F344/NSIc (open squares; $n = 4$) and Hiss (filled circles; $n = 5$). ***C***, Spike amplitudes of the first (left) and last (right) action potentials elicited versus the injected current for F344/NSIc ($n = 4$) and Hiss ($n = 5$) hippocampal bipolar neurons. ***D***, Half-width of the first action potentials and spike decrement for F344/NSIc ($n = 4$) and Hiss ($n = 5$) hippocampal bipolar neurons elicited by 45 pA (left) and 95 pA of current injection (right). The spike decrement was calculated as the percentage of the last spike amplitude divided by the first spike amplitude. Means ± SE are shown. $^*p < 0.01$, $^{**}p < 0.01$ versus F344/NSIc.

which may involve neuronal mechanisms that control respiration and acid–base homeostasis.

Several missense mutations in the $Na_v1.1$ channel have been reported for GEFS+. A couple of studies used recombinant $Na_v1.1$ channels and electrophysiological recordings. They revealed that these mutations may cause either gain-of-function or loss-of-function effects that are consistent with either increased or decreased neuronal excitability (Ragsdale, 2008; Lossin, 2009). Our observations that were based on the electrophysiological analysis of the $Na_v1.1$ channel in heterologously expressed HEK cells indicated that the N1417H missense mutation has a hyperpolarized shift for the voltage dependence of fast inactivation. These results were confirmed for isolated hippocampal interneurons, but not for pyramidal neurons, from Hiss rats. The N1417H missense mutation may decrease the availability of the $Na_v1.1$ channel in inhibitory interneurons, resulting in the partial dysfunction of network inhibition. Interestingly, the M145T mutation of SCN1A linked to simple FS was reported on for a large family (Baulac et al., 2004; Mantegazza et al., 2005; Colosimo et al., 2007). This is consistent with other reports that found a link with the FEB3 locus of FS families (Peiffer et al., 1999; Baulac and Baulac, 2009). The phenotypes and genetic conditions of the Hiss rat seem to be very similar to those reported for simple FS patients of the M145T family. Of note, the M145T mutation causes a partial loss of function.

A persistent current causes neuronal hyperexcitability, for which the channels do not stably inactivate and the sodium currents of mutant cells fail to completely decay to the baseline (Lossin et al., 2002; Meisler and Kearney, 2005; Stafstrom, 2007). Although this abnormal and persistent current represents only a fraction of the peak transient current, it persists long after the transient current has been inactivated. This may profoundly affect neuronal excitability. For our heterologous expression system of HEK cells, the N1417H missense mutation resulted in a slightly but significantly increased persistent current compared with the wild-type channel. This persistent sodium current was confirmed for hippocampal bipolar neurons, but not for pyramidal neurons in Hiss rats. The $Na_v1.1$ channel is predominantly expressed in hippocampal interneurons (Yu et al., 2006; Ogiwara et al., 2007) and also is expressed at lower levels in pyramidal neurons (Tang et al., 2009). We could not clarify whether the persistent sodium current can increase or decrease the excitability of hippocampal neurons. In fact, the combination of opposing biophysical properties, namely the predicted gain and loss of channel activity, has been reported for GEFS+ and related epileptic syndrome-associated SCN1A mutations (Lossin et al., 2002; Rhodes et al., 2005; Ohmori et al., 2006). Our current-clamp recordings clearly showed a reduction in the action potential amplitude for the hippocampal interneurons of Hiss rats. A larger reduction was observed with increasing injected current. This may be associated with enhanced susceptibility to febrile seizures for Hiss rats because of the reduced inhibition of GABAergic interneurons. The resulting dysfunction of network

inhibition can hyperactivate excitatory pyramidal neurons during acute hyperthermia. We could not, however, rule out that other sodium channels, such as $Na_v1.3$ channels, may affect the firing activities of the hippocampus of the mutant rats.

In conclusion, our studies, which used a rat model of FS, revealed that the impaired biophysical properties of hippocampal interneurons contribute to susceptibility to FS among rats. Hiss rats can be used to test the effects of preventative new drugs against FS, FS+, and/or associated epilepsy.

References

Baulac S, Baulac M (2009) Advances on the genetics of mendelian idiopathic epilepsies. Neurol Clin 27:1041–1061.

Baulac S, Gourfinkel-An I, Picard F, Rosenberg-Bourgin M, Prud'homme JF, Baulac M, Brice A, LeGuern E (1999) A second locus for familial generalized epilepsy with febrile seizures plus maps to chromosome 2q21-q33. Am J Hum Genet 65:1078–1085.

Baulac S, Gourfinkel-An I, Nabbout R, Huberfeld G, Serratosa J, Leguern E, Baulac M (2004) Fever, genes, and epilepsy. Lancet Neurol 3:421–430.

Beckh S, Noda M, Lübbert H, Numa S (1989) Differential regulation of three sodium channel messenger RNAs in the rat central nervous system during development. EMBO J 8:3611–3616.

Ben-Ari Y, Holmes GL (2006) Effects of seizures on developmental processes in the immature brain. Lancet Neurol 5:1055–1063.

Chen K, Baram TZ, Soltesz I (1999) Febrile seizures in the developing brain result in persistent modification of neuronal excitability in limbic circuits. Nat Med 5:888–894.

Colosimo E, Gambardella A, Mantegazza M, Labate A, Rusconi R, Schiavon E, Annesi F, Cassulini RR, Carrideo S, Chifari R, Canevini MP, Canger R, Franceschetti S, Annesi G, Wanke E, Quattrone A (2007) Electroclinical features of a family with simple febrile seizures and temporal lobe epilepsy associated with SCN1A loss-of-function mutation. Epilepsia 48:1691–1696.

Dravet C, Bureau M, Oguni H, Fukuyama Y, Cokar O (2005) Severe myoclonic epilepsy in infancy: Dravet syndrome. Adv Neurol 95:71–102.

Dubé C, Richichi C, Bender RA, Chung G, Litt B, Baram TZ (2006) Temporal lobe epilepsy after experimental prolonged febrile seizures: prospective analysis. Brain 129:911–922.

Dubé CM, Brewster AL, Richichi C, Zha Q, Baram TZ (2007) Fever, febrile seizures and epilepsy. Trends Neurosci 30:490–496.

Dzhala VI, Talos DM, Sdrulla DA, Brumback AC, Mathews GC, Benke TA, Delpire E, Jensen FE, Staley KJ (2005) NKCC1 transporter facilitates seizures in the developing brain. Nat Med 11:1205–1213.

Fukuda M, Morimoto T, Nagao H, Kida K (1997) Clinical study of epilepsy with severe febrile seizures and seizures induced by hot water bath. Brain Dev 19:212–216.

Gong B, Rhodes KJ, Bekele-Arcuri Z, Trimmer JS (1999) Type I and type II Na^+ channel alpha-subunit polypeptides exhibit distinct spatial and temporal patterning, and association with auxiliary subunits in rat brain. J Comp Neurol 412:342–352.

Hirabayashi M, Kato M, Aoto T, Sekimoto A, Ueda M, Miyoshi I, Kasai N, Hochi S (2002) Offspring derived from intracytoplasmic injection of transgenic rat sperm. Transgenic Res 11:221–228.

Hodgkin AL, Katz B (1949) The effect of temperature on the electrical activity of the giant axon of the squid. J Physiol 109:240–249.

Holtzman D, Obana K, Olson J (1981) Hyperthermia-induced seizures in the rat pup: a model for febrile convulsions in children. Science 213:1034–1036.

Klauenberg BJ, Sparber SB (1984) A kindling-like effect induced by repeated exposure to heated water in rats. Epilepsia 25:292–301.

Lossin C (2009) A catalog of SCN1A variants. Brain Dev 31:114–130.

Lossin C, Wang DW, Rhodes TH, Vanoye CG, George AL Jr (2002) Molecular basis of an inherited epilepsy. Neuron 34:877–884.

Mani KS, Mani AJ, Ramesh CK (1974) Hot-water epilepsy—a peculiar type of reflex epilepsy: clinical and EEG features in 108 cases. Trans Am Neurol Assoc 99:224–226.

Mantegazza M, Gambardella A, Rusconi R, Schiavon E, Annesi F, Cassulini RR, Labate A, Carrideo S, Chifari R, Canevini MP, Canger R, Franceschetti S, Annesi G, Wanke E, Quattrone A (2005) Identification of an Nav1.1 sodium channel (SCN1A) loss-of-function mutation associated with familial simple febrile seizures. Proc Natl Acad Sci U S A 102:18177–18182.

Mashimo T, Yanagihara K, Tokuda S, Voigt B, Takizawa A, Nakajima R, Kato M, Hirabayashi M, Kuramoto T, Serikawa T (2008) An ENU-induced mutant archive for gene targeting in rats. Nat Genet 40:514–515.

Meisler MH, Kearney JA (2005) Sodium channel mutations in epilepsy and other neurological disorders. J Clin Invest 115:2010–2017.

Moser E, Mathiesen I, Andersen P (1993) Association between brain temperature and dentate field potentials in exploring and swimming rats. Science 259:1324–1326.

Mulley JC, Scheffer IE, Petrou S, Dibbens LM, Berkovic SF, Harkin LA (2005) SCN1A mutations and epilepsy. Hum Mutat 25:535–542.

Nakayama J (2009) Progress in searching for the febrile seizure susceptibility genes. Brain Dev 31:359–365.

Oakley JC, Kalume F, Yu FH, Scheuer T, Catterall WA (2009) Temperature- and age-dependent seizures in a mouse model of severe myoclonic epilepsy in infancy. Proc Natl Acad Sci U S A 106:3994–3999.

Ogiwara I, Miyamoto H, Morita N, Atapour N, Mazaki E, Inoue I, Takeuchi T, Itohara S, Yanagawa Y, Obata K, Furuichi T, Hensch TK, Yamakawa K (2007) $Na_v1.1$ localizes to axons of parvalbumin-positive inhibitory interneurons: a circuit basis for epileptic seizures in mice carrying an *Scn1a* gene mutation. J Neurosci 27:5903–5914.

Ohmori I, Kahlig KM, Rhodes TH, Wang DW, George AL Jr (2006) Nonfunctional SCN1A is common in severe myoclonic epilepsy of infancy. Epilepsia 47:1636–1642.

Peiffer A, Thompson J, Charlier C, Otterud B, Varvil T, Pappas C, Barnitz C, Gruenthal K, Kuhn R, Leppert M (1999) A locus for febrile seizures (FEB3) maps to chromosome 2q23–24. Ann Neurol 46:671–678.

Ragsdale DS (2008) How do mutant Nav1.1 sodium channels cause epilepsy? Brain Res Rev 58:149–159.

Rhodes TH, Vanoye CG, Ohmori I, Ogiwara I, Yamakawa K, George AL Jr (2005) Sodium channel dysfunction in intractable childhood epilepsy with generalized tonic-clonic seizures. J Physiol 569:433–445.

Romijn HJ, Hofman MA, Gramsbergen A (1991) At what age is the developing cerebral cortex of the rat comparable to that of the full-term newborn human baby? Early Hum Dev 26:61–67.

Sadleir LG, Scheffer IE (2007) Febrile seizures. BMJ 334:307–311.

Satishchandra P (2003) Hot-water epilepsy. Epilepsia 44 [Suppl 1]:S29–S32.

Scheffer IE, Berkovic SF (1997) Generalized epilepsy with febrile seizures plus. A genetic disorder with heterogeneous clinical phenotypes. Brain 120:479–490.

Schuchmann S, Schmitz D, Rivera C, Vanhatalo S, Salmen B, Mackie K, Sipilä ST, Voipio J, Kaila K (2006) Experimental febrile seizures are precipitated by a hyperthermia-induced respiratory alkalosis. Nat Med 12:817–823.

Stafstrom CE (2007) Persistent sodium current and its role in epilepsy. Epilepsy Curr 7:15–22.

Sugawara T, Mazaki-Miyazaki E, Ito M, Nagafuji H, Fukuma G, Mitsudome A, Wada K, Kaneko S, Hirose S, Yamakawa K (2001) Nav1.1 mutations cause febrile seizures associated with afebrile partial seizures. Neurology 57:703–705.

Tang B, Dutt K, Papale L, Rusconi R, Shankar A, Hunter J, Tufik S, Yu FH, Catterall WA, Mantegazza M, Goldin AL, Escayg A (2009) A BAC transgenic mouse model reveals neuron subtype-specific effects of a generalized epilepsy with febrile seizures plus (GEFS+) mutation. Neurobiol Dis 35:91–102.

Ullal GR, Satishchandra P, Shankar SK (1996) Hyperthermic seizures: an animal model for hot-water epilepsy. Seizure 5:221–228.

Wu J, Javedan SP, Ellsworth K, Smith K, Fisher RS (2001) Gamma oscillation underlies hyperthermia-induced epileptiform-like spikes in immature rat hippocampal slices. BMC Neurosci 2:18.

Yanagihara K, Mizuuchi K (2002) Mismatch-targeted transposition of Mu: a new strategy to map genetic polymorphism. Proc Natl Acad Sci U S A 99:11317–11321.

Yu FH, Mantegazza M, Westenbroek RE, Robbins CA, Kalume F, Burton KA, Spain WJ, McKnight GS, Scheuer T, Catterall WA (2006) Reduced sodium current in GABAergic interneurons in a mouse model of severe myoclonic epilepsy in infancy. Nat Neurosci 9:1142–1149.

OPEN ACCESS Freely available online

PLoS one

Generation of Knockout Rats with X-Linked Severe Combined Immunodeficiency (X-SCID) Using Zinc-Finger Nucleases

Tomoji Mashimo[1]*, Akiko Takizawa[1], Birger Voigt[1], Kazuto Yoshimi[1], Hiroshi Hiai[2], Takashi Kuramoto[1], Tadao Serikawa[1]

1 Institute of Laboratory Animals, Graduate School of Medicine, Kyoto University, Kyoto, Japan, **2** Shiga Medical Center for Adult Disease, Moriyama, Japan

Abstract

Background: Although the rat is extensively used as a laboratory model, the inability to utilize germ line-competent rat embryonic stem (ES) cells has been a major drawback for studies that aim to elucidate gene functions. Recently, zinc-finger nucleases (ZFNs) were successfully used to create genome-specific double-stranded breaks and thereby induce targeted gene mutations in a wide variety of organisms including plants, drosophila, zebrafish, etc.

Methodology/Principal Findings: We report here on ZFN-induced gene targeting of the rat interleukin 2 receptor gamma (*Il2rg*) locus, where orthologous human and mouse mutations cause X-linked severe combined immune deficiency (X-SCID). Co-injection of mRNAs encoding custom-designed ZFNs into the pronucleus of fertilized oocytes yielded genetically modified offspring at rates greater than 20%, which possessed a wide variety of deletion/insertion mutations. ZFN-modified founders faithfully transmitted their genetic changes to the next generation along with the severe combined immune deficiency phenotype.

Conclusions and Significance: The efficient and rapid generation of gene knockout rats shows that using ZFN technology is a new strategy for creating gene-targeted rat models of human diseases. In addition, the X-SCID rats that were established in this study will be valuable *in vivo* tools for evaluating drug treatment or gene therapy as well as model systems for examining the treatment of xenotransplanted malignancies.

Citation: Mashimo T, Takizawa A, Voigt B, Yoshimi K, Hiai H, et al. (2010) Generation of Knockout Rats with X-Linked Severe Combined Immunodeficiency (X-SCID) Using Zinc-Finger Nucleases. PLoS ONE 5(1): e8870. doi:10.1371/journal.pone.0008870

Editor: Ellen A. A. Nollen, University Medical Center Groningen, Netherlands

Received November 12, 2009; **Accepted** January 4, 2010; **Published** January 25, 2010

Funding: This study was supported in part by a grant-in-aid for cancer research from the Ministry of Health, Labour, and Welfare. The funders had no role in study design, data collection and analysis, decision to publish, or preparation of the manuscript.

Competing Interests: The authors have declared that no competing interests exist.

* E-mail: tmashimo@anim.med.kyoto-u.ac.jp

Introduction

Although several strategies are available for producing a wide variety of genomic alterations in the mouse, the same cannot be said of the rat. Rat ES cells [1,2] and induced pluripotent stem cells (iPS) [3,4] are available, but the culture conditions for these cells and the methodology for inducing homologous recombination are imperfect [5]. Rat spermatogonial stem cells (SSC) have also been isolated and cultivated *in vitro* but their yield proved unsatisfactory in terms of their ability to undergo homologous recombination [6,7]. Besides these methods which are based on the *in vitro* genetic engineering of pluripotent stem cells, transposon-mediated mutagenesis [8] and N-ethyl-N-nitrosourea (ENU) mutagenesis [9,10] have been used with some success for producing mutations in the rat genome. We recently reported on a high-throughput gene-driven strategy which uses the mutagen ENU and the Mu-transposition reaction (MuT-POWER) to rapidly detect induced mutations. This was in addition to our investigation of intracytoplasmic sperm injection (ICSI) for recovering heterozygous genotypes of interest out of a large sperm cell repository [11,12]. However, even if a large number of mutant strains already exists or may potentially be available, targeted modification or disruption of specific DNA regions is difficult to achieve. Even in the case of our gene-driven strategy, X-linked mutations are impossible to obtain because of the breeding protocol which is used [11].

Recently, a novel gene-targeting technology which employs zinc-finger nucleases (ZFNs) has been proven to work successfully in plants, *Caenorhabditis elegans*, frogs, drosophila, zebrafish, and human ESCs and iPSCs [13,14,15]. ZFNs are chimeric proteins that consist of a specific DNA-binding domain which is made of tandem zinc finger-binding motifs that are fused to a non-specific cleavage domain of the restriction endonuclease *Fok*I. ZFNs can create site-specific double-stranded breaks which are repaired via non-homologous end joining (NHEJ), a process that results in the arbitrary addition or deletion of base pairs. Consequently, repair by NHEJ is mutagenic and results in a knockout. Recently, it was reported that a single injection of DNA or messenger RNA that encodes specific ZFNs into one-cell transgenic rat embryos that express GFP could lead to a high frequency of animals that do not express the transgenic marker as a consequence of homologous recombination at the GFP site [16]. Here, we report on an experiment that involved using ZFN technology. The aim of the experiment was to inactivate the gene that encodes the interleukin 2 receptor gamma (*Il2rg*), which is essential for signaling by interleukins such as IL-2, IL-4, IL-7, IL-9, IL-15, and IL-21. In

addition, the gene is involved in the X-linked form of severe combined immunodeficiency (X-SCID), one of the most common forms of human SCID [17,18]. A major motivation for performing this experiment was the observation that although SCID mouse animal models are the most commonly used in research on drug development, an X-SCID immunodeficient rat model would complement mouse models through the additional advantage of being employed for testing the pharmacodynamics and toxicity of potential therapeutic compounds. Following the results of research involving *Prkdc* SCID [19,20] and *Il2rg* X-SCID mice [21,22,23], *Il2rg* X-SCID rats should have a very low level of NK cell activity and thereby make xenotransplantation more successful.

Results

Injection of *Il2rg* ZFN-encoding mRNA into rat embryos

Of 443 ZFN-injected embryos, 230 (51.9%) were transferred into the oviducts of pseudopregnant female rats, and 54 (24.3%) of these embryos were successfully carried to term as shown in Figure 1a, b and Table 1. Sequence analysis of the ZFN target site of these 54 founder animals revealed that 5 males and 8 females (24.1%) carried a variety of mutations including from 3 to1,097 bp deletions and a 1 bp insertion in the region which overlapped the ZFN target site as seen in Figure 1c and Figure S1. Four out of five of the males carried different biallelic mutations at the *Il2rg* locus despite them only having one X chromosome. This suggests that mosaicism was induced by the ZFN treatment, a situation which is frequently observed in the DNA of transgenic founders. Three of the affected females had a monoallelic homozygous mutation, four had heterologous or mosaicism biallelic mutations, and the remainder had three different mosaic mutations. The normal F344-allele was not found in the affected founder animals. Most of these mutations were expressed as frameshifts or splicing errors and resulted in no or very little IL2RG mRNA being expressed as shown in Figure 1d probably due to nonsense-mediated decay. Western blotting with antibodies against the C-terminal domain of

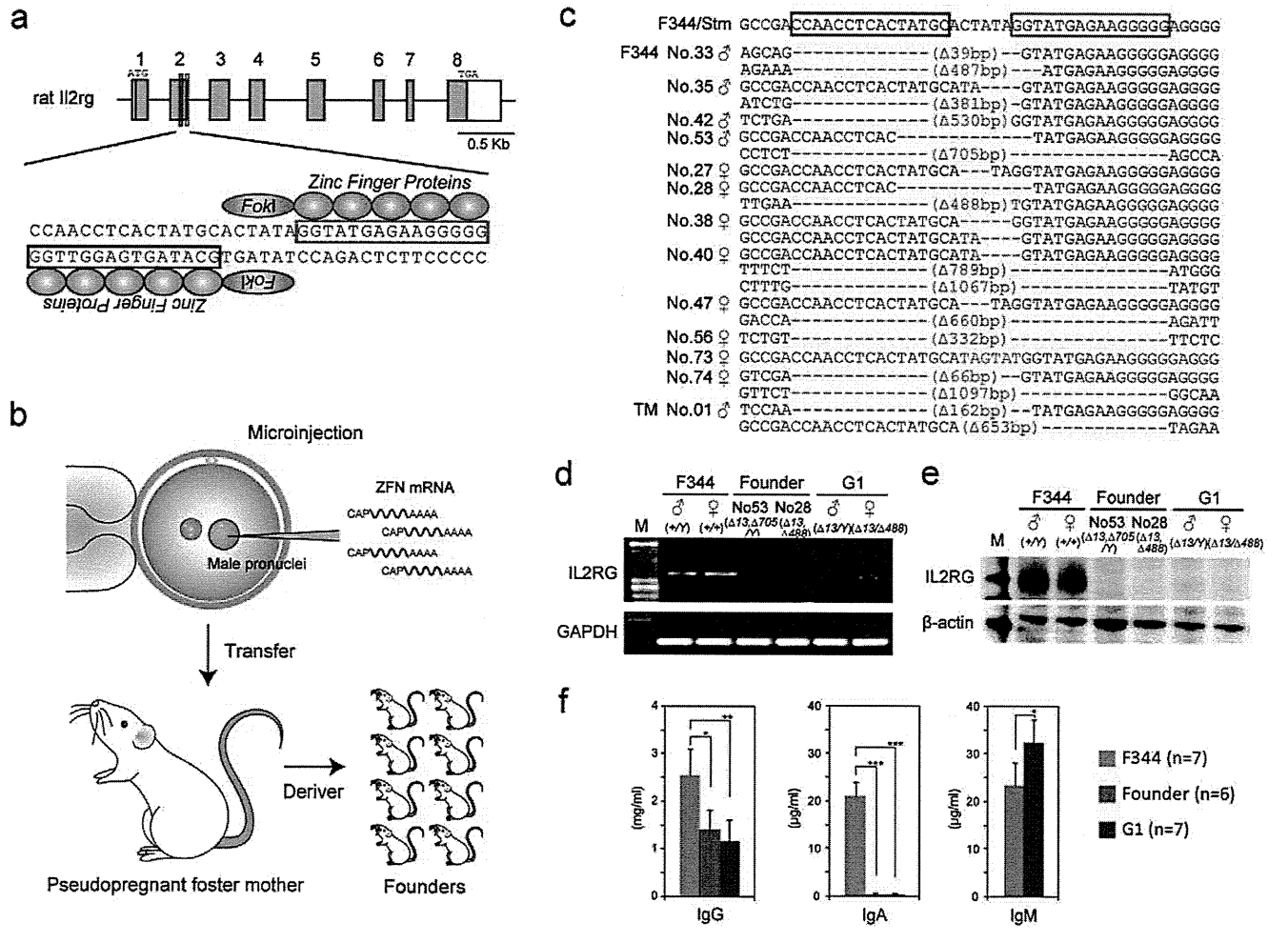

Figure 1 Injection of *Il2rg* ZFN-encoding mRNA into rat embryos induced targeted loss-of-function mutations. (a) Schematic representation of the rat *Il2rg* gene. Exons are represented as blue boxes. Regions used to design the ZFN templates are printed in red for the left ZFN and green for the right ZFN. The magnified views illustrate the binding sites for the ZFN pairs. Please see Figure S4 for further details. (b) Schematic representation of the method used for ZFN-targeted mutagenesis in rat embryos. (c) Sequencing assay for ZFN-induced mutations in the *Il2rg*-targeted region. Multiple deletions or insertions depicted using red dashes or letters, respectively, are aligned along the wild-type sequences shown on the top line. (d) RT-PCR analysis of IL2RG mRNA expression in the spleen of control F344, founder (G0), and G1 rats. GAPDH expression was used as an internal control. (e) Western blotting for IL2RG protein in the spleen of control F344, founder (G0), and G1 rats. β-actin was used as a loading control. (f) ELISA for serum IgG, IgA, and IgM levels in control F344, founder (G0), and G1 rats. *P<0.01, **P<0.001, and ***P<0.0001, indicated for each group in comparison with control F344 for independent sample Student t-tests.
doi:10.1371/journal.pone.0008870.g001

Table 1. Injection of ZFN-encoding mRNA into fertilized oocytes.

Strain	Oocyte state	Injected oocytes	Transferred oocytes (%)	Born (%)	Mutants (%)
F344/Stm	Fresh	234	32 (-)	♂2,♀5 (21.9)	♀2 (28.6)
	Cryopreserved[a]		57 (-)	♂8,♀10 (31.6)	♀2 (11.1)
	Fresh	182	129 (68.3)	♂16,♀11 (20.9)	♂4,♀4 (29.6)
TM/Kyo	Fresh	27	12 (44.4)	♂1,♀1 (16.7)	♂1 (50.0)
Total		**443**	**230 (51.9)**	**♂27,♀27 (24.3)**	**♂5,♀8 (24.1)**

[a]Injected oocytes were cultured in KRB overnight and cryopreserved at the two-cell stage.
doi:10.1371/journal.pone.0008870.t001

IL2RG did not reveal any protein in the founder animals as seen in Figure 1e.

To clarify whether the ZFNs only induced mutations in the targeted region, we checked 16 sites that showed a high rate of similarity with the targeted site at the sequence level with no more than 6 to 7 bp mismatches as illustrated in Table S1. Insertions or deletions were not observed at any of these off-target sites among the 13 ZFN-modified founders. This confirms that ZFNs can be reliably and efficiently used to produce mutant alleles at loci of interest. Although we cannot exclude the possibility that the ZFNs may have cleaved unknown off-target sites, such undesired mutations can subsequently be easily excluded from the genome of the carrier animals by backcrossing to the parental strain or another background strain.

Germ line transmission of ZFN-modified genetic changes

To assess the transmission of ZFN-modified genetic changes to the next generation, we crossed the founder animals with the background strain F344/Stm as depicted in Table S2. All 38 offspring consisting of 18 males and 20 females that were obtained from the founder females mated with the F344 males had one of the maternal mutations. This indicates that ZFN-induced mutations were faithfully transmitted through the germ line. In the offspring that were obtained from the founder males, there were two cases where only one of the paternal bialleles was transmitted or both alleles were transmitted. This suggests that mosaicism occurred not only in somatic cells but also in the germ line of the founder animals. PCR analysis of genomic DNA isolated from several types of tissues indicated that somatic mosaicism occurred in the progenitors but not in their offspring as shown in Figure S2.

We intercrossed the G0 founders to produce hemizygous males (*Il2rg*$^{-}$/*Y*) and homozygous females (*Il2rg*$^{-}$/*Il2rg*$^{-}$) for the ZFN-induced mutation listed in Table S3 to characterize the immunodeficient phenotypes of the X-SCID rats. The hemizygous males and homozygous females appeared normal at birth and developed well as shown in Figure 2a. RT-PCR and Western blot assays was performed on these G1 rats and the results showed a complete loss of expression of the *Il2rg* gene as detailed in Figures 1d, e. ELISA for serum immunoglobulin (Ig) levels revealed reduced IgG, diminished IgA, and increased IgM levels in the G1 rats as noted in Figure 1f.

Characterization of *Il2rg*-deficient X-SCID rats

Gross and microscopic analyses at five weeks of age showed that the X-SCID rats underwent abnormal lymphoid development as depicted in Figure 2. The thymus of X-SCID rats was extremely hypoplastic as seen in Figure 2b and consisted of an epithelial rudiment without any lymphocytes as seen in Figure 2d. The spleen was moderately decreased in size as noted in Figure 2c, and the white pulp was severely hypoplastic and the red pulp contained myeloid cells as shown in Figure 2f. Peripheral lymph nodes and Peyer's patches were not identified by necropscopy. In the peripheral blood (PB) profiles, the numbers of white blood cells (WBCs) was reduced compared to those of control rats as detailed in Table S4. Differential counts of WBCs showed a dramatic decrease in leukocytes in the X-SCID rats (Table S5). Flow cytometry analysis of cell populations isolated from PB, bone marrow (BM), and the spleen also revealed a dramatic decrease in the number of the lymphocytes as seen in Figure 2h and Figure S3. The number of $CD4^{-}CD8^{+}$ T-cells was markedly diminished and the number of $CD4^{+}CD8^{-}$ T-cells was decreased although some cells were present in PB, BM and the spleen. The numbers of $CD3^{-}CD45RA^{+}$ B-cells and $CD3^{-}CD161a^{+}$ NK cells were markedly diminished in PB and BM, but some cells were present in the spleen. Heterozygous females exhibited normal lymphoid development and were indistinguishable from normal control females (data not shown).

Xenotransplantation of human tumor cells

These immunodeficient phenotypes of the X-SCID rats were very similar to those of the previously reported X-SCID mice and were characterized by a nearly complete lack of T-cells, B-cells and NK cells [21,22,23]. Since X-SCID mice cannot reject transplanted tissues from other species including humans, we tested *Il2rg*-deficient rats as a host for xenotransplantation of human ovarian cancer tumor cells. All X-SCID rats developed tumors within 14 days after injection of the cells (6/6, 100%), while control F344 rats showed no tumor growth (0/6, 0%) as seen in Figure 3a, b. The tumors were confirmed by histological analysis as depicted in Figure 3c and by PCR with primers that were used to amplify the human MHC class II DQB2 region (data not shown). These observations illustrate the impaired immune system function of X-SCID rats and suggest that the animals may be important models for cancer and transplantation research.

Discussion

In this study, we proved that targeted gene disruption using ZFN technology works well and provides for several advantages and possibilities when used in rats. First and foremost, knockout rats can be created in a four- to six-month time frame and with high efficiency at more than 20%. This is more favorable than the ES cell-based method for mice that usually takes 12–18 months. Given the high rate of germ line transmission, preliminary phenotypic analysis can be performed on G1 animals after intercrossing the initial G0 founders, thereby saving time and effort. Second, gene-targeting with ZFNs does not seem to be strain-dependent (unpublished data) and accordingly can be performed with any inbred strain. This is of great advantage

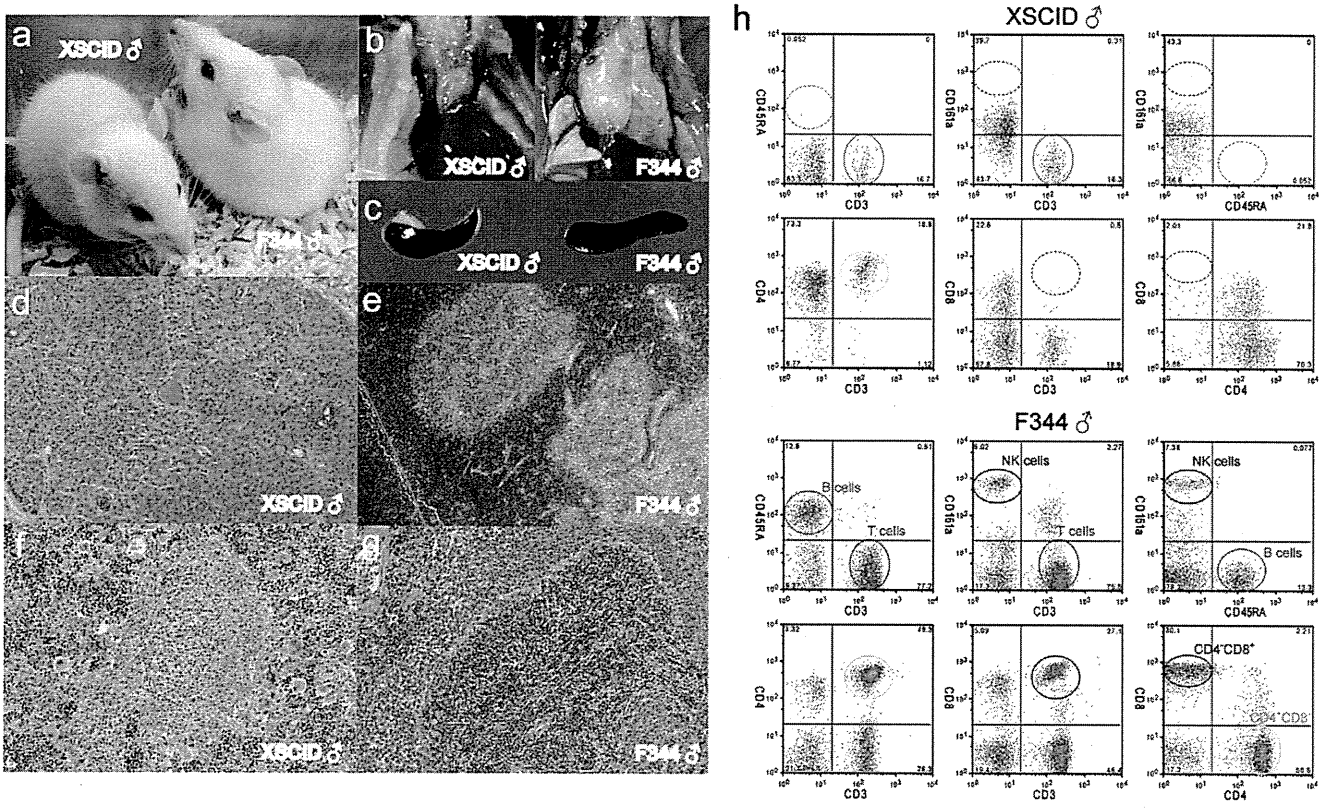

Figure 2 Abnormal lymphoid development in X-SCID rats. (a) Photograph of five week-old male X-SCID (*Il2rg*$^{-}$/*Y*) and F344 (+/*Y*) rats. (b) Thymus of X-SCID and F344 rats. (c) Spleen of X-SCID and F344 rats. (d, e) Histological analysis of the thymus of X-SCID (X40) and F344 (X40) rats. The thymus of the X-SCID rat was severely hypoplastic and consisted of an epithelial cell sheet. (f, g) Histological analysis of the spleen of X-SCID (X100) and F344 (X100) rats. In the X-SCID spleen, the white pulp was virtually devoid of lymphocytes and the red pulp was occupied by a variety of myeloid elements. (h) Dot plots representing CD3, CD45RA and CD161a for differentiation of T-, B- and NK cell sub-populations, and CD3, CD4 and CD8 for demarcation of T-cell sub-populations in peripheral blood lymphocyte cells. The numbers shown in the quadrants are mean percentages. The circled areas indicate cell populations that are referred to in the text.
doi:10.1371/journal.pone.0008870.g002

since other techniques like ENU mutagenesis differ in their efficiency when used with different strains. This provides a straight forward strategy for directly employing targeted gene disruption in the existing strain, thereby bypassing tedious and time-consuming backcrossing steps that generally take two to three years to complete. Third, ZFNs can be used to induce a wide variety of allelic changes covering small or wide deletions or insertions. They may be used to produce frameshifts or small in-frame deletions such as the 3-bp deletion that we observed. Given the reports on successful ZFN-targeted gene modification or correction by homologous recombination in mammalian cell cultures [15,24,25], it should be feasible to archive targeted knock-in technologies that have thus been far inaccessible without rat ES cells. Finally, since ZFN technology does not rely on using species-specific embryonic stem cell lines, it should be possible to adapt it to other mammalian species such as pigs, cattle, and monkeys, where it is possible to harvest and manipulate fertilized embryos.

The X-SCID rats established in this study provide not only a valuable *in vivo* model for evaluating drug treatment or gene therapy approaches, but also a system for assaying novel anticarcinogenic effects on transplanted malignancies. There is a growing need for animal models with which to carry out *in vivo* studies using human cells, tissues or organs as chimeras such as humanized models [26,27,28]. X-SCID and SCID mice homozygous for *Il2rg*- and *Prkdc*- alleles with a non-obese diabetic background are a powerful tool for the xenotransplantation of human tissues or potentially human ES/iPS cells. This could lead to advances in our understanding of human hematopoiesis, immunology, cancer biology, infectious diseases, and regenerative medicine [29,30,31]. Humanized rats, if generated by ZFN technology, could be powerful tools for pre-clinical testing during drug development and be better models in various fields of translational research.

Materials and Methods

Animals

All animal care and experiments conformed to the Guidelines for Animal Experiments of Kyoto University, and were approved by the Animal Research Committee of Kyoto University. F344-*Il2rg*^{tm1Kyo} X-SCID rats are deposited at the National Bio Resource Project for the Rat in Japan (www.anim.med.kyoto-u.ac.jp/nbr).

ZFN constructs

Custom-designed ZFNs plasmids for the rat *Il2rg* gene were obtained from Sigma-Aldrich. The design, cloning, and validation of the ZFNs was performed by Sigma-Aldrich [32]. ZFN design involved using an archive of pre-validated two-finger and one-finger modules [32,33]. The target region was scanned for positions where modules exist in the archive. This allowed the fusion of two or three such molecules to generate a five-finger

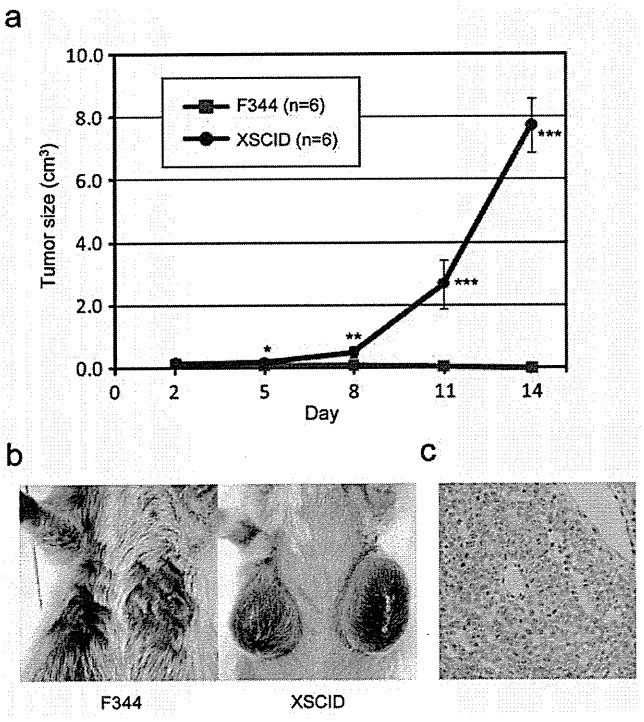

Figure 3 Tumor development from the xenotransplantation of human ovarian cancer cells. (a) Growth curve of tumor development after subcutaneous injection of A2780 human ovarian cancer cells in F344 and X-SCID rats. *P<0.01, **P<0.001, and ***P<0.0001, indicated in comparison with control F344. (b) The tumors became large and grew quickly about 11 days after injection in X-SCID rats but not in F344 rats. (c) Histology of the xenotransplanted tumors that formed in X-SCID rats (X400). No lymphocytic infiltration was detected in the tumors.
doi:10.1371/journal.pone.0008870.g003

protein that recognizes a 15 bp site on the top strand and the fusion of two to three different modules that recognize a 15 bp site on the bottom strand that lies 5–6 bp away. Measurements of ZFNs for gene disruption activity were performed using the Surveyor endonuclease (CEL-1) assay as described elsewhere [34]. Final candidate ZFNs were designed to recognize a site within the boundary between exon 2 and intron 2 of the *Il2rg* gene as shown in Figure S4.

Microinjection of ZFN mRNA

To prepare ZFN mRNA, ZFN-encoding expression plasmids were linearized with *Xho*I and extracted with phenol-chloroform by the standard method. Messenger RNA was transcribed *in vitro* using a MessageMax^{TM} T7 mRNA transcription kit (Epicentre) and polyadenylated using a A-Plus^{TM} Poly(A) polymerase tailing kit (Epicentre). The resulting mRNA was purified using a MEGAClear^{TM} kit (Epicentre) and finally resuspended in RNase-free water at 10 ng/μl for each ZFN. Approximately 2–3 pL of capped mRNA were injected into the male pronuclei of zygotes by the same method that was used to microinject DNA. Pronuclear stage embryos were collected from F344/Stm and TM/Kyo females six weeks of age that had been super-ovulated by injecting them with eCG (Serotropin, Asuka Pharmaceutical Co.) and hCG (Gonatropin, Asuka Pharmaceutical Co.). They were mated with males of the same respective strain. The mRNA solution was injected and embryos were cultured in KRB at 37.5°C with 5% CO_2 and 95% humidified air to promote their recovery. The embryos that survived were transferred to the oviduct of pseudopregnant females (Crlj:WI, 8–12wks).

Analysis of genome editing at ZFN target sites

Genomic DNA was extracted from the tail, brain, heart, and liver using a GENEXTRACTOR TA-100 automatic DNA purification system (Takara). PCR for each was carried out in a total volume of 15 μl under the following conditions for 35 cycles: 94°C for 3 min for 1 cycle, 94°C for 30 sec, 60°C for 30 sec, and 72°C for 1 min. The final reaction mixture for each contained 100 ng of genomic DNA, 200 μM of each dNTP, 1.0 mM $MgCl_2$, 0.66 μM of each primer, and 0.4 U of Taq DNA polymerase (GibcoBRL).

For editing the ZFN cleavage site in the genome at the *Il2rg* locus, three primer sets were designed to amplify small 292-bp, middle 1509-bp, and large 3158-bp fragments as shown in Figure S4. The PCR products were directly sequenced using the BigDye terminator v3.1 cycle sequencing mix and the standard protocol for an Applied Biosystems 3130 DNA Sequencer. The products were also subcloned into the pCR4-TOPO vector (Invitrogen), and plasmid DNA was prepared and sequenced on a 3130 DNA Sequencer. All new sequence data is deposited in GenBank (GU294902-GU294925).

Off-target site analysis

Off-target sites with the highest degree of similarity were identified by searching the rat genome (RGSCv3.4) for matches with the consensus sequence of each ZFP with appropriate spacing of 5–6 bp. A list of these target sites is provided in Supplementary Table 1. PCR primers were designed to flank the off-target sites as detailed in Table S6. Reactions were performed for the founder animals and the PCR products were directly sequenced on the 3130 DNA Sequencer.

RT-PCR and Western blotting

Total RNA was extracted using Isogen reagent (Nippon Gene) from the spleen of five week-old rats. First strand cDNA was synthesized from 5 μg of total RNA that had been treated using DNase by using the oligo(dT)12–18 primer and SuperscriptII reverse transcriptase (Invitrogen). PCR was performed with the primers for *Il2rg* described in Figure S4 and with the *Gapdh* 5′-GGCACAGTCAAGGCTGAGAATG-3′ and 5′-ATGGTGGT-GAAGACGCCAGTA-3′. Western blotting was carried out using the cell lysates from the spleens of five week-old rats by the standard method. Signals were detected with antibodies against rat IL2RG (M-20, Santa Cruz Biotechnology) and β-actin (AC-40, Sigma Aldrich).

Immunofluorescence and histological analyses

Complete necroscopy examinations were performed on five week-old *Il2rg*-deficient and wild-type male and female rats. Peripheral blood specimens were collected from the caudal vena cava. Serum immunoglobulin (Ig) levels were measured by enzyme-linked immunosorbent assay (ELISA) using Rat IgG, IgA and IgM ELISA Quantitation kits (Bethyl Laboratories). Blood parameters for a complete blood cell count, a WBC differential, and a reticulocyte count were measured using ADVIA 2120 flow cytometry (Block Scientific). For histopathology, tissues were fixed in Bouin's fluid and embedded in paraffin. The embedded tissues were then sectioned at 5–7 μm thickness at room temperature and stained with hematoxylin and eosin to permit evaluation by light microscopy.

Flow cytometric analyses of cell populations isolated from bone marrow, the spleen and peripheral blood were carried out using IOTest Anti-Rat CD3-FITC/CD45RA-PC7/CD161a-APC (Beckman Coulter) to differentiate T-, B- and NKcell sub-populations and IOTest Anti-Rat CD3-FITC/CD4-PC7/CD8-APC (Beckman Coulter) to enumerate T-cell sub-populations. Anti-CD45 monoclonal antibodies (Beckman Coulter) were used for the intracellular staining of lymphocytes. Mouse IgM, IgG1 and IgG2a antibodies (Beckman Coulter) were used as isotype-matched controls. The cell samples were treated with FcR-blocking reagent (Miltenyi Biotec) for 10 minutes, stained with the fluorochrome-conjugated antibodies for 30 minutes, and washed three times with PBS/10% FCS. Stained cell samples were analyzed with a four-color FACS flow cytometer (FACSCalibur, Becton Dickinson) using CellQuest software (Becton Dickinson).

Tumor cell xenotransplantation

The human ovarian cancer cell line A2780 was purchased from the European Collection of Cell Cultures (ECACC). Cells were cultured in RPMI1640 medium (GIBCO) with 10% heat-inactivated FBS (Hyclone). Subcutaneous injections of 2×10^5 A2780 cells with Matrigel (Becton Dickinson) were performed on five week-old female rats. Tumors were measured by length (a) and width (b) in millimeters using calipers, and tumor volumes (V) were calculated according to the relationship $V=ab^2/2$, where a was the longer of the two measurements. Human-specific PCR primers were designed to amplify major histocompatibility complex class II DQ beta 2 (HLA-DQB2) at exon 4 as follows: 5′-CCTAGG-GTGGTCAGACTGGA-3′ and 5′-AAAATCCCCCAAAACA-AAGG-3′.

Supporting Information

Figure S1 PCR analysis of 13 mutant founders for the zinc-finger nuclease (ZFN) target site. For the analysis of the ZFN target site at the *Il2rg* locus, three primer sets were used to amplify small (a, 292-bp), middle (b, 1509-bp), and large (c, 3158-bp) fragments for PCR. See Figure S4 for further details. PCR fragments were electrophoresed through a 1-4% agarose gel. M: DNA molecular weight marker ϕX174-*Hae*III digest.
Found at: doi:10.1371/journal.pone.0008870.s001 (9.19 MB TIF)

Figure S2 PCR analysis of genomic DNA isolated from several tissues. Three primer sets were used to amplify small (a, 292-bp), middle (b, 1509-bp), and large (c, 3158-bp) fragments for PCR. See Figure S4 for further details. Genomic DNA (T: tail, B: brain, H: heart, L: liver) was used as a template for PCR in zinc-finger nuclease-modified founders (numbers 28, 35, 40, and 53) and G1 rats. PCR fragments were electrophoresed through a 1–4% agarose gel. M: DNA molecular weight marker ϕX174-*Hae*III digest or Lambda DNA-*Hind*III digest.
Found at: doi:10.1371/journal.pone.0008870.s002 (6.28 MB TIF)

Figure S3 Flow cytometric analysis of bone marrow lymphocyte cells (a) and spleen lymphocyte cells (b) from five-week-old F344 and X-SCID rats. Dot plots represent CD3, CD45RA, and CD161a for discrimination of T-, B-, and NK cell subpopulations; and CD3, CD4, and CD8 for demarcation of T cell subpopulations. The numbers shown in quadrants are mean percentages. Circled areas indicate cell populations referred to in the text.
Found at: doi:10.1371/journal.pone.0008870.s003 (6.66 MB TIF)

Figure S4 Zinc-finger nuclease pairs designed against the *Il2rg* locus and primer sequences used for PCR analysis for the *Il2rg* gene. Each exon is underlined. The start codon is indicated by a red box. The three primer sets (small, middle, and large) used for the PCR analysis of *Il2rg* are shown by boxes. Primers used for the RT-PCR are shown as cDNA.
Found at: doi:10.1371/journal.pone.0008870.s004 (3.32 MB TIF)

Table S1 Potential zinc-finger nuclease off-target sites.
Found at: doi:10.1371/journal.pone.0008870.s005 (0.14 MB DOC)

Table S2 Backcrossing of zinc-finger nuclease-modified founders to F344/Stm rats.
Found at: doi:10.1371/journal.pone.0008870.s006 (0.16 MB DOC)

Table S3 Intercrossing of zinc-finger nuclease-modified founders between males and females.
Found at: doi:10.1371/journal.pone.0008870.s007 (0.08 MB DOC)

Table S4 Peripheral blood profiles of *Il2rg*-deficient (X-SCID) rats.
Found at: doi:10.1371/journal.pone.0008870.s008 (0.09 MB DOC)

Table S5 Differential counts of the white blood cells of *Il2rg*-deficient (X-SCID) rats.
Found at: doi:10.1371/journal.pone.0008870.s009 (0.07 MB DOC)

Table S6 Primer sequences for zinc-finger nuclease off-target analysis.
Found at: doi:10.1371/journal.pone.0008870.s010 (0.14 MB DOC)

Acknowledgments

This study was supported in part by a Grant-in-aid for Cancer Research from the Ministry of Health, Labour and Welfare. We thank JL Guénet for critical discussion, and Y Kunihiro, F Tagami, and S Ishida for their assistance with the experiment.

Author Contributions

Conceived and designed the experiments: TM BV TS. Performed the experiments: TM AT KY HH TK. Analyzed the data: TM. Wrote the paper: TM.

References

1. Li P, Tong C, Mehrian-Shai R, Jia L, Wu N, et al. (2008) Germline competent embryonic stem cells derived from rat blastocysts. Cell 135: 1299–1310.
2. Buehr M, Meek S, Blair K, Yang J, Ure J, et al. (2008) Capture of authentic embryonic stem cells from rat blastocysts. Cell 135: 1287–1298.
3. Liao J, Cui C, Chen S, Ren J, Chen J, et al. (2009) Generation of induced pluripotent stem cell lines from adult rat cells. Cell Stem Cell 4: 11–15.
4. Li W, Wei W, Zhu S, Zhu J, Shi Y, et al. (2009) Generation of rat and human induced pluripotent stem cells by combining genetic reprogramming and chemical inhibitors. Cell Stem Cell 4: 16–19.
5. Voigt B, Serikawa T (2009) Pluripotent stem cells and other technologies will eventually open the door for straightforward gene targeting in the rat. Dis Model Mech 2: 341–343.
6. Ryu BY, Kubota H, Avarbock MR, Brinster RL (2005) Conservation of spermatogonial stem cell self-renewal signaling between mouse and rat. Proc Natl Acad Sci U S A 102: 14302–14307.
7. Shinohara T, Kato M, Takehashi M, Lee J, Chuma S, et al. (2006) Rats produced by interspecies spermatogonial transplantation in mice and in vitro microinsemination. Proc Natl Acad Sci U S A 103: 13624–13628.